Scales, Growth Rates, and Spectral Fluxes of Baroclinic Instability in the Ocean

Citation: Tulloch, Ross et al. "Scales, Growth Rates, and Spectral Fluxes of Baroclinic Instability in the Ocean." Journal of Physical Oceanography 41 (2011): 1057-1076. © 2011 American Meteorological Society.

As Published: http://dx.doi.org/10.1175/2011jpo4404.1

Publisher: American Meteorological Society

Persistent URL: http://hdl.handle.net/1721.1/66964

Version: Final published version: final published article, as it appeared in a journal, conference proceedings, or other formally published context

Scales, Growth Rates, and Spectral Fluxes of Baroclinic Instability in the Ocean

ROSS TULLOCH, JOHN MARSHALL, AND CHRIS HILL

Department of Earth, Atmospheric and Planetary Sciences, Massachusetts Institute of Technology, Cambridge, Massachusetts

K. SHAFER SMITH

Center for Atmosphere Ocean Science, New York University, New York, New York

(Manuscript received 23 November 2009, in final form 15 January 2011)

ABSTRACT

An observational, modeling, and theoretical study of the scales, growth rates, and spectral fluxes of baroclinic instability in the ocean is presented, permitting a discussion of the relation between the local instability scale; the first baroclinic deformation scale $R_{\rm def}$; and the equilibrated, observed eddy scale. The geography of the large-scale, meridional quasigeostrophic potential vorticity (QGPV) gradient is mapped out using a climatological atlas, and attention is drawn to asymmetries between midlatitude eastward currents and subtropical return flows, the latter of which has westward and eastward zonal velocity shears. A linear stability analysis of the climatology, under the ''local approximation,'' yields the growth rates and scales of the fastest-growing modes. Fastest-growing modes on eastward-flowing currents, such as the Kuroshio and the Antarctic Circumpolar Current, have a scale somewhat larger (by a factor of about 2) than $R_{\rm def}$. They are rapidly growing (e folding in 1–3 weeks) and deep reaching, and they can be characterized by an interaction between interior QGPV gradients, with a zero crossing in the QGPV gradient at depth. In contrast, fastest-growing modes in the subtropical return flows (as well as much of the gyre interiors) have a scale smaller than $R_{\rm def}$ (by a factor of between 0.5 and 1), grow more slowly (e-folding scale of several weeks), and owe their existence to the interaction of a positive surface QGPV gradient and a negative gradient beneath.

These predictions of linear theory under the local approximation are then compared to observed eddy length scales and spectral fluxes using altimetric data. It is found that the scale of observed eddies is some 2–3 times larger than the instability scale, indicative of a modest growth in horizontal scale. No evidence of an inverse cascade over decades in scale is found. Outside of a tropical band, the eddy scale varies with latitude along with but somewhat less strongly than $R_{\rm def}$.

Finally, exactly the same series of calculations is carried out on fields from an idealized global eddying model, enabling study in a more controlled setting. Broadly similar conclusions are reached, thus reinforcing inferences made from the data.

1. Introduction

Satellite altimetry indicates that much of the mesoscale in the World Ocean is dominated by eddies that scale roughly with the first baroclinic (BC) deformation radius $R_{\rm def}$ and have about 50 times the kinetic energy (KE) of the mean flow (see, e.g., Stammer 1997). But how these eddies are generated and what sets their equilibrated scale remain open questions. The ocean is a complex turbulent fluid subject to surface and tidal forcing as well as internal flow instabilities. It has been proposed (Frankignoul and Müller 1979) and debated (Large et al. 1991; Stammer and Wunsch 1999) that stochastic wind forcing can generate the midocean eddies directly. However, Ferrari and Wunsch (2009) note that the approximate agreement between linear theory and observations support the view that baroclinic instability of available potential energy (APE) in the mean currents is the main eddy kinetic energy source. Baroclinic instability appears to be ubiquitous, with the sloping isopycnals in the main thermocline storing roughly 1000 times more APE than the KE associated with its thermal-wind current shear (Gill et al. 1974).

The full instability problem in ocean gyres is a difficult one. In this paper, we will adopt the local approximation,

Corresponding author address: Ross Tulloch, Department of Earth, Atmospheric and Planetary Sciences, Massachusetts Institute of Technology, 77 Massachusetts Avenue, Cambridge, MA 02139.
E-mail: tulloch@mit.edu

DOI: 10.1175/2011JPO4404.1

which represents a vast simplification of the full problem. The local approximation assumes that each lateral location of the ocean is a local, horizontally homogeneous patch. Within each patch, the eddies are assumed to be the weakly nonlinear response to instability of the local and steady mean flow and stratification. Gill et al. (1974) and Robinson and McWilliams (1974) used the local approximation to show that midocean currents are baroclinically unstable on spatial and temporal scales, consistent with observations. Arbic (2000) further concluded that local baroclinic instability seems to be a plausible mechanism for midocean eddy generation.

However, the local approximation is clearly not universally appropriate and ignores many dynamical possibilities. First, the steady assumption neglects eddy feedback onto the mean flow (Farrell and Ioannou 1999; Flierl and Pedlosky 2007) as well as the propagation of eddies into and out of regions of high and low baroclinic growth rate. Other dynamics that play a role in eddy formation include the radiation of instabilities from boundary currents into the interior (Kamenkovich and Pedlosky 1996; Hristova et al. 2008), weakly nonlinear growth of unstable modes (Hart 1981; Pedlosky 1981), sensitivity to nonzonal flow instabilities (Spall 2000; Arbic and Flierl 2004; Smith 2007a), nonparallel flow instabilities (Pedlosky 1987), barotropic (BT) instabilities of horizontally varying mean flows, and strongly nonlinear turbulent dynamics (Held and Larichev 1996). However, for better or worse, the horizontal locality assumption underlies most mesoscale ocean eddy theories and parameterizations in ocean general circulation models, and linear theory at least provides a well-defined prediction.

The goal in this paper is simply to compare the spatial and temporal scales predicted by local linear theory with the fully developed nonlinear eddy field in the World Ocean, neglecting the possible dynamical processes that may occur between the two. The scales of baroclinic instability expected from linear theory are computed analogously to Smith (2007b)[1] and Killworth and Blundell (2007) but using the hydrographic atlas of Forget (2010). The most unstable scales are then compared with observed energy-containing scales inferred from diagnoses of spectral energy fluxes derived from surface satellite altimetry using the method reported in Scott and Wang (2005). The baroclinic instability analysis and spectral flux calculations are then repeated in an eddying simulation with full ocean dynamics, constant wind forcing, and idealized orography.

We find that, in both ocean observations and the eddying model simulation, in highly energetic predominantly eastward-flowing currents, such as the Antarctic Circumpolar Current (ACC), Gulf Stream, and Kuroshio, the instability scale is larger than $R_{\rm def}$ and penetrates deep into the water column. The quasigeostrophic potential vorticity (QGPV) gradient in these eastward-flowing regions tends to change sign at a depth of ~1 km. By contrast, the baroclinic instability of the gentler, westward return flows[2] occurs on horizontal scales smaller than $R_{\rm def}$ and is surface intensified, consistent with driving by a QGPV reversal within ~100 to 200 m of the surface. These broad tendencies can be understood as follows: For baroclinic instability to occur, the QGPV gradient must reverse sign in the interior or have the opposite sign of the buoyancy gradient at the upper surface (Charney and Stern 1962; Pedlosky 1964). The mean states in the classic models of baroclinic instability constructed by Charney (1947) and Phillips (1954) can be thought of as idealizations of the two typical observed mean gradient configurations. Instability in the two-layer model of Phillips (1954) is driven by the mean QGPV gradient sign reversal between the two layers, whereas the Charney (1947) model instability is driven by an interaction of the mean surface temperature gradient with a constant interior PV gradient β; the former is analogous to the eastward current regimes, whereas the latter is analogous to the westward current regimes (though with β replaced by the mean thermal-wind QGPV gradient). Here, we classify these two types of baroclinic instabilities as ''Phillips like'' and ''Charney like,'' respectively.

These generalized definitions allow us to characterize two qualitatively distinct regimes, but of course typical oceanic velocity profiles contain a mix of both surface and nonconstant interior gradients, so these generalizations do not always apply. Currents with mixed shear, such as in the subtropical return flows are not well represented by two-mode or two-layer models because they contain both positive and negative interior QGPV shear as well as an upper boundary condition that opposes the interior shear beneath it. However, three-layer QG models have been used to show that elevated eddy energy in the 20°–30° latitude bands is due to baroclinic instability of sloping isopycnals (Halliwell et al. 1994; Qiu 1999; Kobashi and Kawamura 2002; Qiu et al. 2008). In the calculations presented here, we adopt 50 vertical levels and so adequately resolve key features of the flow and do not need to calibrate vertical model parameters.

[1] Some of the results reported in Smith (2007b) are in error because of a gridding mistake in the computation, as discussed in appendix A.

[2] ''Westward return flows'' refers to regions typical of the 20°–30° latitudes which are predominantly westward between about 100-m and 1-km depths and have easterly shear at depth and westerly shear near the surface (i.e., mixed shear in Fig. 3).

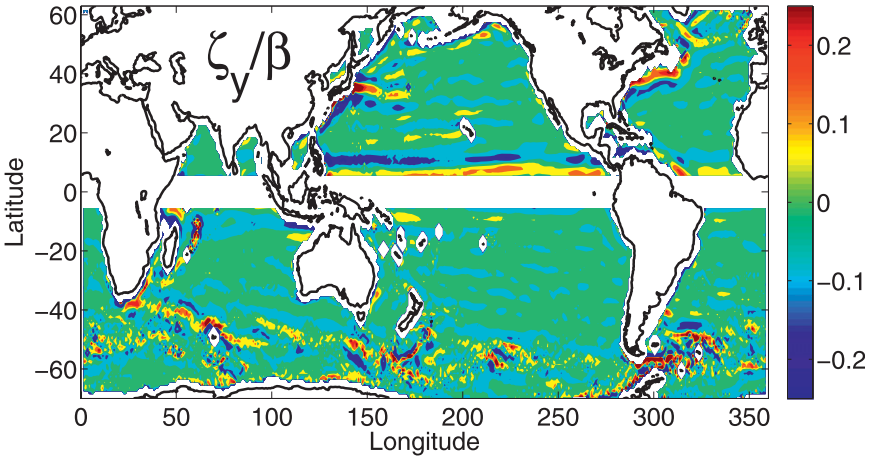

FIG. 1. Relative vorticity at the surface in the OCCA state estimate, nondimensionalized by the local planetary PV gradient β. The relative vorticity is small compared to β almost everywhere.

Our paper is organized as follows: In section 2, the climatology of the ocean's large-scale meridional QGPV gradient is mapped out using the hydrographic Ocean Comprehensible Atlas (OCCA; Forget 2010). In section 3, baroclinic growth rates and the horizontal scales of maximum growth rate are computed using zonal and meridional mean currents from the atlas at chosen points and are also mapped globally. In section 4, the results of linear theory are compared to the observed energy-containing scale and spectral fluxes of (geostrophic) KE computed from Archiving, Validation, and Interpretation of Satellite Oceanographic data (AVISO) gridded satellite altimetry (Le Traon et al. 1998). The scale at which the kinetic energy spectral flux crosses zero, which is called the energy injection scale, is then compared with the scale of maximum baroclinic growth rate. In section 5, the analyses of sections 3 and 4 are performed on an eddying simulation on an aquaplanet. In section 6, the results are interpreted in terms of instability and geostrophic turbulence theory and conclusions are drawn.

2. Climatology of the meridional potential vorticity gradient

As described in the introduction, the QGPV gradient is a diagnostic from which to infer the geography of instability. Here, we focus on the meridional QGPV gradient in predominantly zonal flows and ignore nonzonal mean flows. Note however that nonzonal mean flows characterize significant regions of the ocean. Nonzonal mean flows yield zonal mean PV gradients Q_x, and are thus more unstable than zonal flows because the planetary vorticity gradient does not provide a restoring force to zonal PV perturbations (Pedlosky 1987; Walker and Pedlosky 2002). Moreover, baroclinic instabilities generated by nonzonal mean flows are very effective at generating baroclinic turbulence (Spall 2000; Arbic and Flierl 2004) because of a strong nonlinear feedback between eddy generation and eddy scale and anisotropy (Smith 2007a). Here we focus on flows that are relatively zonal, such as the ACC, boundary current extensions, and subtropical return flows.

The large-scale meridional QGPV gradient, generalized as in Bretherton (1966) to include upper and lower boundary conditions via delta function sheets, is

$$\frac{\partial \tilde{Q}}{\partial y} = \beta - f\frac{\partial s}{\partial z} + \frac{f^2}{N^2}\frac{dU}{dz}\delta_{\text{upper}}, \tag{1}$$

where β is the planetary PV gradient, $s = -b_y/N^2$ is the meridional isopycnal slope, f is the Coriolis parameter, N^2 is the stratification, and δ_{upper} is a delta function at the upper boundary. Note that we have neglected contributions from the lower boundary and from relative vorticity. Our neglect of the relative vorticity of the mean flow is well justified by its small magnitude relative to β, as shown in Fig. 1, computed at the surface from the OCCA.

Various hydrographic ocean atlases are available from which QGPV can be computed. The calculations presented here were performed on the OCCA, which is a 3-yr climatology for 2004–06 on a $1° \times 1°$ horizontal grid with 50 vertical levels (Forget 2010). Altimeter data, satellite sea surface temperature, and Argo profiles are assimilated in a least squares sense using the adjoint of the Massachusetts Institute of Technology GCM (MITgcm; Marshall et al. 1997; Marotzke et al. 1999; Adcroft et al. 2004b). We note that our analysis is insensitive to the particular ocean climatology used, and key results are compared for three different climatologies in appendix A.

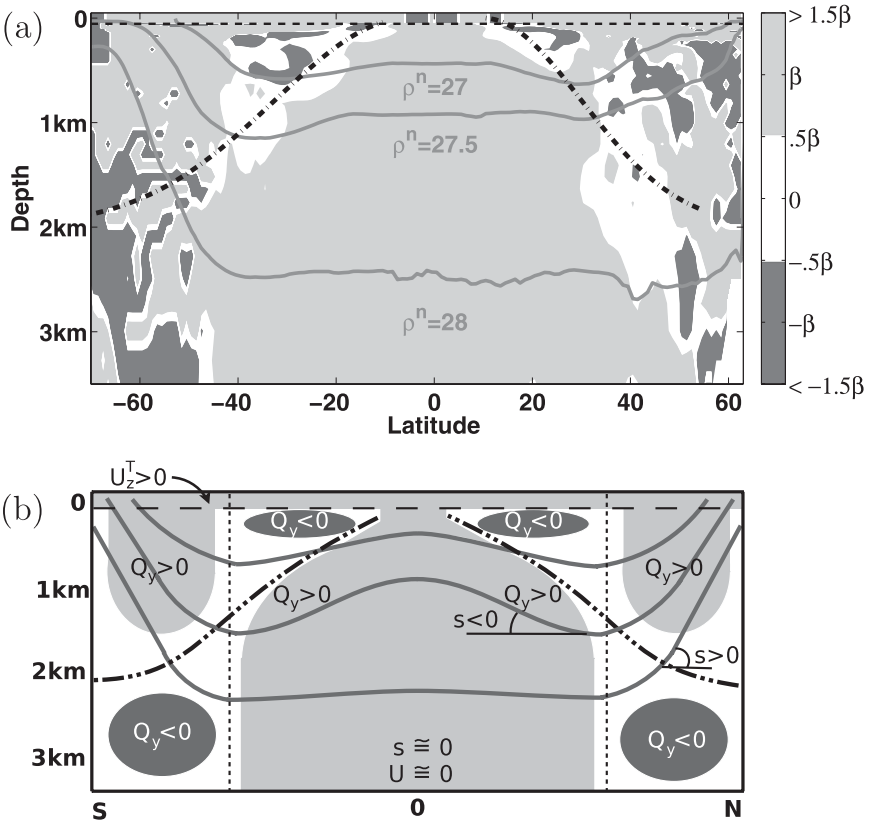

FIG. 2. Zonally averaged cross section of the meridional QGPV gradient (in units of β), from the OCCA. The upper surface gradient U_z is shown above the dashed line evaluated at a depth of 50 m, and gray contours are neutral density. (b) An idealized schematic of the PV gradients with isopycnals (solid gray lines) sloping up toward the equator (pole) at low (high) latitudes. Light (dark) shaded regions indicate $Q_y > 0$ ($Q_y < 0$), and the dashed–dotted line indicates $Q_y = 0$. Poleward-sloping isopycnals are associated with deep PV gradient zero crossing, whereas equatorward-sloping isopycnals are associated with zero crossing shallower than the thermocline. The δ-function surface contribution above the dashed line assumes the equator is more buoyant than the poles at the surface. See text for details.

Figure 2a shows a cross section of the zonally averaged QGPV gradient, Eq. (1), computed from the OCCA. In the computation, it is assumed that the geostrophic zonal velocity is in thermal-wind balance with the meridional density gradient. The QGPV gradient is normalized by β and plotted in three-tone grayscale. The white shading indicates regions where the meridional QGPV gradient is near zero (i.e., $-\beta/2 \le Q_y \le \beta/2$). The light gray indicates positive regions ($Q_y > \beta/2$), and the dark gray indicates negative regions ($Q_y < -\beta/2$). The surface gradient U_z is indicated above the dashed line at 50-m depth. The light and dark gray regions can in some places, particularly the ACC, be on the order of $\pm 100\beta$. Superimposed are gray contours of zonally averaged neutral density (γ^n = 27, 27.5, and 28) to give an indication of thermocline structure. The dashed–dotted curve is a visual guide to indicate the depth of the zero crossings of the QGPV gradient.

There is an asymmetry in the distribution of Q_y between regions where isopycnals slope up toward the poles (i.e., eastward currents) and where isopycnals slope up toward the equator in the thermocline (i.e., currents with mixed shear, westerly above easterly, as sketched in Fig. 3). This asymmetry is more pronounced in the Southern Hemisphere because eastward jets in the Northern Hemisphere are not as extensive, being confined to western margins of the gyres. The Northern Hemisphere also contains convective regions north of 50°N, which create negative QGPV gradients below stratification minima (i.e., at a few hundred meters depth). A schematic diagram of an idealized QGPV gradient (that ignores the convective regions in the Northern Hemisphere) is shown in Fig. 2b. If deep currents are weak, then, given the thermal-wind equation $fU_z = -\overline{b}_y = N^2 s$, flow above will be directed eastward ($U > 0$), where isopycnals (solid

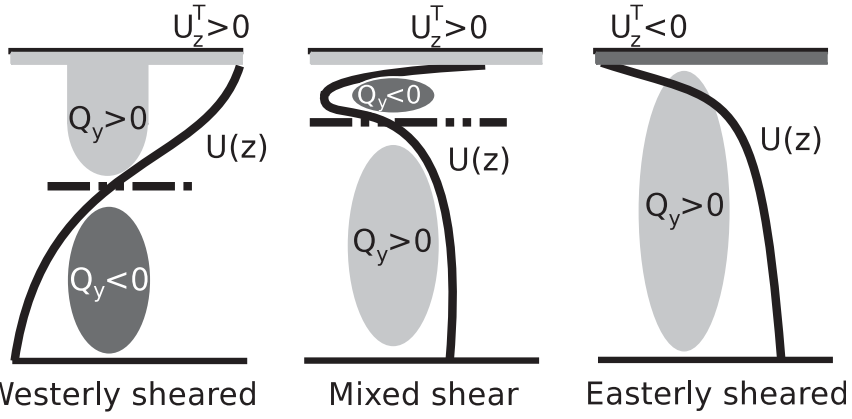

FIG. 3. Schematic of typical zonal velocity profiles in westerly, mixed, and easterly sheared mean flows. The curve indicates $U(z)$, and the horizontal dashed line indicates approximately the height at which the QGPV gradient is zero, assuming negligible planetary PV gradient. The surface shear is opposed to the PV gradient immediately beneath in the mixed and easterly sheared profiles.

gray lines) slope up toward the pole ($s > 0$ in the Northern Hemisphere), and directed westward ($U < 0$), where they slope up toward the equator ($s < 0$). The vertical extent of the thermocline is greater in eastward-flowing regions relative to westward-flowing regions. The vertical distribution of Q_y depends on the manner in which isopycnal slopes vary in the vertical. Isopycnal slopes tend to have a maximum at middepth in the thermocline, leading to a reversal in sign of Q_y at middepth, marked by the dashed–dotted line. The broad patterns in the sign of Q_y are indicated by light gray ($Q_y > 0$) and dark gray ($Q_y < 0$) shading. In addition, there is a delta function contribution in Eq. (1) associated with surface boundary conditions, which has a positive sign ($U_z > 0$) at all latitudes (except the deep tropics) because the meridional buoyancy gradient at the surface is generally negative. This surface condition has little effect on regions where isopycnals slope up toward the pole, but it is an important driver of baroclinic instability in subtropical return flow regions that have $Q_y < 0$ beneath.

Figure 3 zooms in on idealized profiles of zonal velocity in typical westerly, mixed, and easterly sheared flows. Note that westerly sheared profiles represent regions such as the ACC, Kuroshio, and Gulf Stream; mixed shear profiles represent gyre return flows (at approximately ±20°–30°); and easterly sheared profiles represent north and south equatorial countercurrents (at approximately ±10°–20°). Charney instabilities are not possible at the upper surface in a westerly sheared flow as depicted in Fig. 3: the shear has the same sign as the upper surface gradient and so the only instability that can occur is analogous to a two-layer Phillips instability. However, in the mixed shear flow shown in Fig. 3, the upper surface gradient opposes the QGPV gradient just below it, so Charney instabilities near the surface are possible. As discussed in the conclusions, we hypothesize that such Charney instabilities make surface quasigeostrophic (SQG) dynamics (Held et al. 1995; Lapeyre 2009) more relevant in such mixed shear flows compared to westerly sheared flows. Moreover, near-surface Phillips instabilities can also occur because of the shallow zero crossing of the interior QGPV gradient. Finally, the easterly sheared flow depicted in Fig. 3 contains no interior QGPV gradient zero crossings; therefore, instability can only occur through the interaction of the negative surface gradient with the positive QGPV gradient beneath it.

3. Local instability analysis

Local baroclinic growth rates, scales of maximum instability, and vertical structures of unstable modes are computed by solving the linearized QG equations about the local climatological streamfunction $\Psi(z) = V(z)x - U(z)y$ and stratification $N^2(z)$,

$$\partial_t q + J(\Psi, q) + J(\psi, \beta y + \Gamma\Psi) = 0, \quad -H < z < 0,$$
$$\partial_t b + J(\Psi, b) + J(\psi, f\partial_z \Psi) = 0, \quad z = -H, 0, \quad (2)$$

where $\Gamma = \partial_z(f^2/N^2\partial_z)$ is the vortex stretching operator, $b = f\partial\psi/\partial z$ is buoyancy, $q = (\nabla^2 + \Gamma)\psi$ is the eddy QGPV, and rigid lid and a flat bottom have been assumed. The vertical is discretized into 50 levels and derivatives are computed using centered differences in the same way as in Tulloch et al. (2009), which is based on the method used in Smith (2007b). The discretized version of Eq. (2) becomes a generalized eigenvalue problem when a wave solution of the form $\psi = \Phi(z)e^{i(\mathbf{K}\cdot\mathbf{x} - \omega t)}$ is assumed, where $\mathbf{K} = k\mathbf{i} + \ell\mathbf{j}$ is

the wavenumber vector, ω is the eigenvalue, and $\Phi(z)$ is the eigenvector.

In the discussion that follows, the wavenumber of the fastest-growing mode $K_{\rm bci}$ is compared to the local deformation wavenumber $K_{\rm def}$, which is defined as the square root of the first nonzero eigenvalue of the vertical-mode equation,[3]

$$\frac{d}{dz}\left[\frac{f^2}{N^2}\frac{d\phi(z)}{dz}\right] = -K_{\rm def}^2\phi(z), \tag{3}$$

with upper and lower boundary conditions $d\phi/dz = 0$. Note that, in addition to the thermocline baroclinic instabilities, which are the focus of our attention here, small-scale, surface trapped instabilities at wavenumbers significantly larger than $K_{\rm def}$ also appear in the linear stability analysis. Smith (2007b) argued that, because such surface instabilities do not penetrate far into the thermocline, they are insignificant from the viewpoint of baroclinic conversion of APE to KE. Regardless of the importance of submesoscale instabilities and dynamics, the balanced QG analysis performed here does not properly resolve such instabilities. We therefore choose to limit the wavenumber range considered at each location to $K < 5K_{\rm def}$, where K is the magnitude of the horizontal wavenumber $K = (k^2 + \ell^2)^{1/2}$. We return to this in the discussion.

a. Detailed stability calculations at chosen locations

Figure 4 shows instabilities computed at two eastward-flowing locations and two locations in the subtropics with mixed shear: (39.5°N, 60.5°W) in the Gulf Stream (Figs. 4a–d); (51.5°S, 141.5°E) in the ACC (Figs. 4e–h); (23.5°N, 60.5°W) in the western subtropical North Atlantic (Figs. 4i–l); and (23.5°N, 155.5°E) in the western subtropical North Pacific (Figs. 4m–p). Each row of Fig. 4 shows the neutral density profile; geostrophic zonal (solid line) and meridional (dashed line) current profiles; growth rate ω_i as a function of zonal and meridional wavenumbers (k, ℓ); and the vertical structure of the amplitude of the most unstable wave, whose wavenumber $K_{\rm bci} = (k_{\rm bci}^2 + \ell_{\rm bci}^2)^{1/2}$ is marked by a dot in the third column. Note that the barotropic component of the flow is assumed to be zero, because it does not alter baroclinic growth rates (Smith 2007b). Each of the growth rate plots in the third column presents four contours at equal intervals, spanning the peak growth rate over the domain: wavenumbers have been nondimensionalized by the local deformation wavenumber $K_{\rm def}$. In the fourth column, the numerical value of $K_{\rm bci}/K_{\rm def}$ is also indicated. The peak growth rates at the four locations are 0.053, 0.11, 0.015, and 0.017 days^{-1} (Figs. 4c,g,k,o, respectively), which highlights how unstable the Gulf Stream and ACC are compared to the subtropical flow regions.

1) WESTERLY SHEAR

The two locations in eastward-flowing currents are dominated by instabilities that have a scale $K_{\rm bci}^{-1}$ larger than the deformation radius and extend all the way to the bottom, despite being peaked at the surface. These Gulf Stream and ACC instabilities can be thought of as Phillips instabilities because they can be recovered in a two-layer or two-mode model. The Gulf Stream instability is surface intensified, which is consistent with the surface-intensified stratification there. The amplitude of the ACC instability is largest at the surface but is also bottom intensified, typical of a Phillips instability with constant stratification. The stratification in the ACC is clearly not constant, but it is far less surface intensified than elsewhere in the ocean. Although the ACC instability is not constrained to have zero interior PV gradients, as assumed in the Eady (1949) model, it is worth noting that the growth rate and length scales of the two are very similar. The Eady instability has a peak growth rate of $\omega_{\rm Eady} = 0.31(f/NH)\Delta U$ at a horizontal scale $K_{\rm bci}/K_{\rm def} = 0.51$. The growth rate in Fig. 4g can be compared with that of an Eady mode when the meridional velocity is neglected. Recalling that for constant N^2 the first deformation wavenumber is $K_{\rm def} = \pi f/NH$, then setting $\Delta U = 0.2$ m s^{-1} and $K_{\rm def} = 5.85 \times 10^{-5}$ rad m^{-1} gives $\omega_{\rm Eady} = 0.1$ days^{-1}, which is close to the computed value of 0.11 days^{-1}.

Some unstable growth also occurs at wavenumbers in the corners of the domain in Fig. 4g. This growth is associated with a mode that peaks at very small scales (wavenumber $K_{\rm bci}/K_{\rm def} = 18$) and has virtually zero amplitude at depths shallower than 2 km. We believe that this is a spurious, unphysical numerical mode and not robustly resolved in our calculation because it changes significantly given different vertical discretizations, ocean climatologies, and geographic locations. For example, neighboring locations typically exhibit surface-intensified modes at these small scales rather than bottom-intensified ones. Here, we seek to identify mesoscale instabilities; thus, we restrict our analysis to wavenumbers with magnitude $K < 5K_{\rm def}$ and consider only those that peak inside that wavenumber domain. The scale of the mesoscale instabilities typically peak at a $K_{\rm bci}$ that is within a factor of 2 of $K_{\rm def}$, which is in accordance with the classical

[3] The deformation radius is defined as $R_{\rm def} = K_{\rm def}^{-1}$, and the deformation wavelength is defined as $L_{\rm def} = 2\pi K_{\rm def}^{-1}$. Note that in what follows we also define $L_{\rm bci} = 2\pi K_{\rm bci}^{-1}$

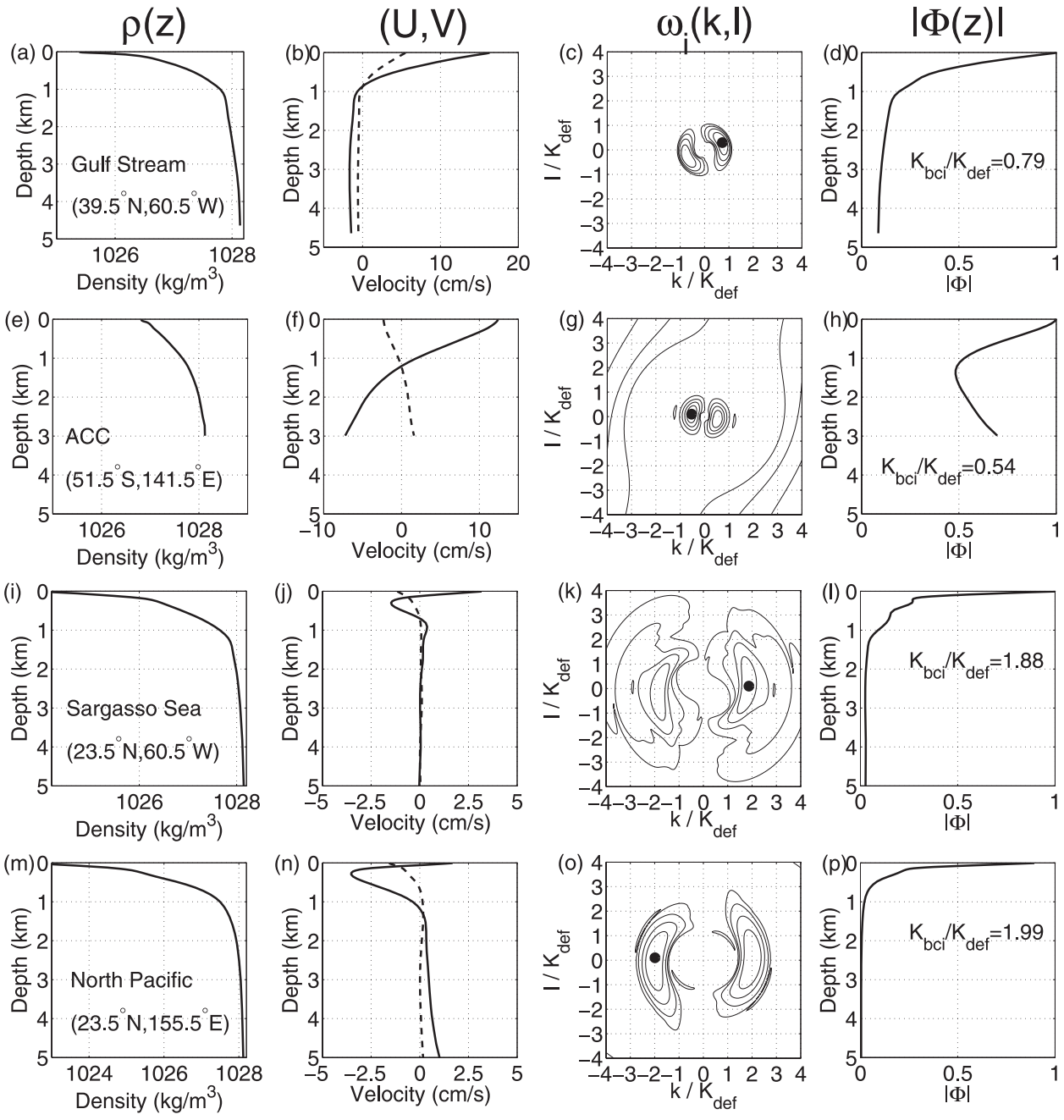

FIG. 4. Local baroclinic instability analysis using the OCCA at four locations: (left)–(right) neutral density, zonal (solid) and meridional (dashed) geostrophic velocity, contours of growth rate ω_i against zonal and meridional wavenumbers, and amplitude profiles of the fastest-growing baroclinic mode, which is located at the wavenumber $\mathbf{K}_{\text{bci}}$ labeled with a dot in the third column.

models of baroclinic instability in geostrophic (Charney 1947; Eady 1949; Phillips 1954; Green 1960) and non-geostrophic (Stone 1966) flows.

2) MIXED SHEAR

In contrast to the two eastward-flowing locations, the subtropical sites with mixed shear (bottom two rows of Fig. 4) are characterized by thermal-wind shears that change sign near the surface. This is because the interior circulation is increasingly directed westward with height but must "join on" to a shear associated with a horizontal density gradient at the surface that is of the opposite sign (i.e., a shear that is directed eastward). The resulting instabilities are associated with a shallow zero crossing in

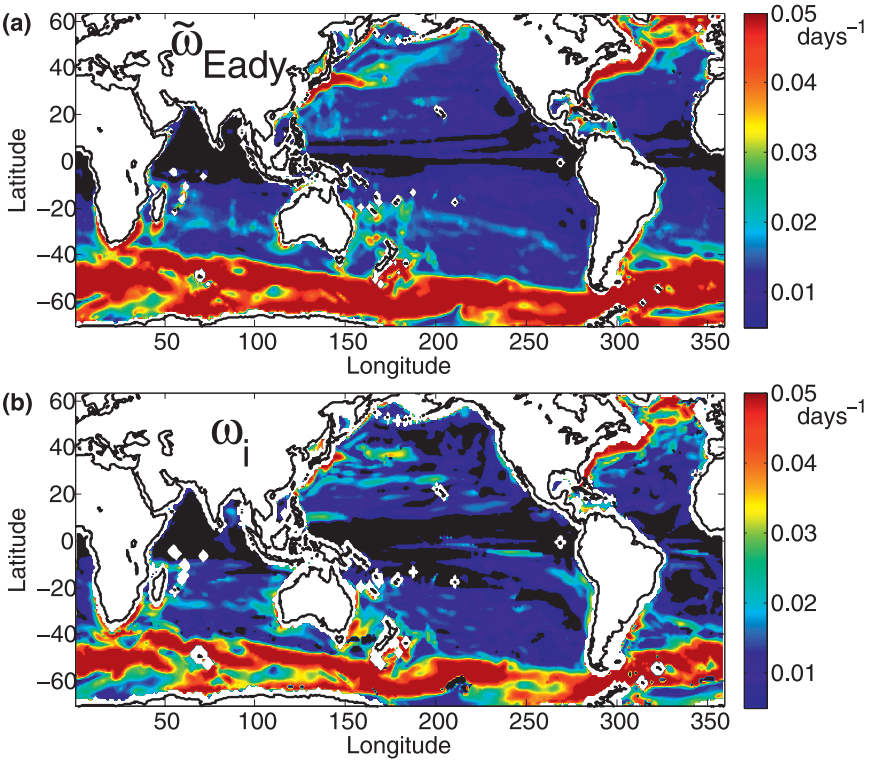

FIG. 5. (a) Inverse Eady time scale $\tilde{\omega}_{\text{Eady}}$ (days^{-1}) and (b) baroclinic growth rate ω_i days^{-1} in the OCCA. Values less than $^1/_{200}$ days^{-1} and locations where no local maximum growth rate is present are shaded black. The coastline is marked by a black contour, and regions where no calculation was made are shaded white.

gradients of QGPV (see Fig. 2): they are weaker and shallower than their westward counterparts and lie at horizontal wavenumbers K_{bci} that are about twice K_{def}. The instability cannot be captured by a two-vertical-mode representation and is either the result of a zero crossing of the QGPV gradient near the surface (near-surface Phillips) or the interaction of the surface gradient with the QGPV gradient just below the surface (Charney like).

The broad geography of baroclinic instability implied by Fig. 2 is evident in Fig. 4: at higher latitudes, where isopycnals slope up toward the pole, the flow is often baroclinically unstable with vertically deep modes at horizontal scales larger than the deformation radius. In contrast at lower latitudes, where isopycnals slope up toward the equator in the thermocline, flows are primarily unstable near the surface at smaller-than-deformation scales. We note in passing that this weaker dependence of the horizontal scale of the fastest-growing mode on deformation scale is consistent with observed eddy length scales found by Scott and Wang (2005) and Chelton et al. (2007). However, the connection between the observed eddy scale and the scale of the fastest-growing mode is far from clear (see the discussion in section 4).

b. Global distribution of growth rates and scales

Global maps and zonal averages of local growth rates and unstable length scales are now presented. At each (latitude, longitude) coordinate, the eigenvalue problem associated with Eq. (2) is solved over 80 × 80 wavenumbers in (k, ℓ) space. Figure 5a shows an estimate of the baroclinic growth rate from the so-called Eady time scale (Visbeck et al. 1997; Smith 2007b). The inverse Eady time scale $\tilde{\omega}_{\text{Eady}}$ is derived by Smith (2007b) by integrating the mean APE $(f^2/2N^2)\Psi_z^2$ both vertically and horizontally over a box, assuming a local mean streamfunction $\Psi = -yU(z) + xV(z)$, to arrive at

$$\tilde{\omega}^2_{\text{Eady}} = \frac{1}{H}\int_{-H}^{0} \frac{f^2}{N^2}\frac{U_z^2 + V_z^2}{6}\, dz \qquad (4)$$

after neglecting the cross terms U_zV_z. The factor of 6 arises from integrating $\Psi_z^2/2$ and, for constant stratification and zonal shear, it conveniently scales to $0.41(f/NH)\Delta U$, which is close to the peak growth rate $0.31(f/NH)\Delta U$ of the Eady (1949) model.

The growth rates computed from the detailed stability analysis, Eq. (2), are shown in Fig. 5b. They are typically

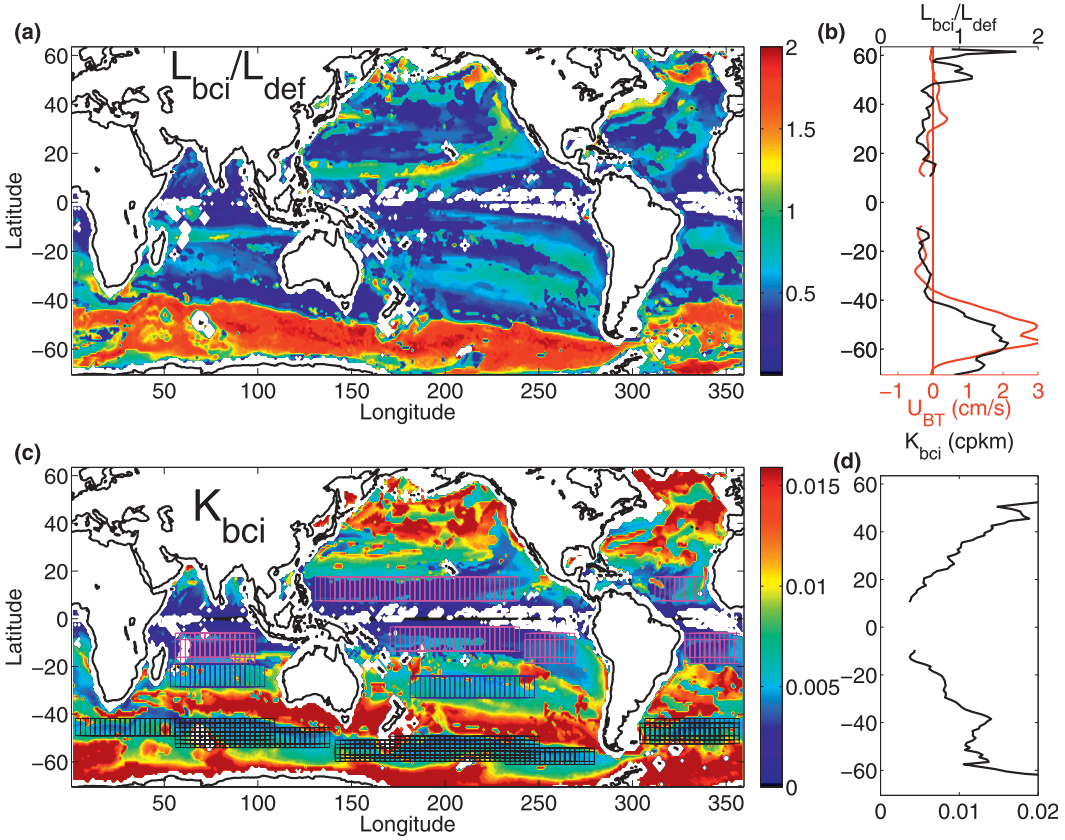

FIG. 6. (a) Map and (b) zonal average of L_{bci}/L_{def}. The red line in (b) is a zonal and vertical average of the zonal velocity (cm s^{-1}), indicating eastward vs westward flow. (c) Map and (d) zonal average of K_{bci} (cycles per kilometer): black (ACC), blue (midgyre), and purple (return flow) boxes denote homogeneous regions about which zonal averages are taken for comparison with spectral fluxes computed from satellite altimetry.

slightly smaller than $\tilde{\omega}_{Eady}$, but the spatial pattern of the two are very similar. The most notable differences between the $\tilde{\omega}_{Eady}$ and the detailed calculation are found at low latitudes. Here, the mean flow is dominated by higher baroclinic modes, which are not well captured by the vertical integral in Eq. (4). At higher latitudes, there is close agreement between ω_i and $\tilde{\omega}_{Eady}$. Note that, in a few regions, such as near the equator in the South Equatorial Current, the growth rate has been set to zero (shaded black) because no growth rate peaks were found within the search domain ($K < 5K_{def}$).

Figure 6 shows maps and zonal averages of L_{bci}/L_{def} (top) and K_{bci} (bottom). The red curve in Fig. 6b is the zonal and vertical average of the zonal velocity (cm s^{-1}). Eastward jet regions in Fig. 6a are typically shaded yellow or red because $K_{bci} < K_{def}$, whereas return flows are typically light blue because $K_{def} < K_{bci} < 2K_{def}$ here. Dark blue regions, which have the smallest baroclinic length scales, correlate well with regions of small growth rate ($\omega_i < 1/200$ days^{-1}). Note that L_{bci} in the ACC appears to be robustly larger than L_{def}. Signatures of large-scale baroclinic instability are also evident in the Gulf Stream and Kuroshio. Gyre interiors, which are only weakly unstable, have a patchy appearance and small baroclinically unstable scales $K_{bci} > K_{def}$.

Finally, the purple, blue, and black boxes superimposed on Fig. 6c indicate regions of approximate homogeneity over which zonal averages will be taken to compare the most baroclinically unstable length scale with the scales of eddies and spectral fluxes computed from altimetry.

4. Diagnosis of observed scales and spectral energy fluxes from altimetry

The scales of the fastest-growing mode computed in the previous section can be compared with eddy length scales and spectral fluxes using satellite altimeter data. Here, we make use of the approach of Scott and Wang (2005) because we are interested in diagnosing the injection scale, the scale of the equilibrated eddy field, and the flux of energy in wavenumber space between them. The calculation of Scott and Wang (2005) is repeated using

interpolated, 1/3° Mercator gridded sea surface height (SSH) AVISO (through 2008). To compute the KE spectrum and spectral energy flux in this way, one takes two-dimensional Fourier transforms over some local box. Because the ocean is not meridionally homogeneous, smaller grids are preferred, but at the risk of not resolving the large scales if the grid is too small. Scott and Wang (2005) investigated the dependence of the flux on the grid size using 32×32, 64×64, and 128×128 grids and found a small but consistent bias toward smaller scales when smaller grid sizes were used. Nevertheless, to maximize the number of samples and keep statistics local, here all spectral flux calculations are performed on 32×32 grids while avoiding the deep tropics, where scales approach the size of the box. Eddy length scales are taken to be the peak of the KE spectrum. See appendix B for a discussion of different measures of eddy scale.

Spectral fluxes

Spectral fluxes are computed identically to the method of Scott and Wang (2005) with the exception that Gibbs phenomena due to nonperiodic data are suppressed using periodic data flipping, instead of a Hamming window. In a comparison test between the two methods, data flipping gave almost identical fluxes to a Hamming window, but with what appeared to be a slightly weaker forward KE fluxes at small scales. As with Scott and Wang (2005) and Schlösser and Eden (2007), the method of Frisch (1995) is used to compute the spectral KE fluxes at the surface. Assuming geostrophic balance and an f plane within each box, the surface velocities are given by $\mathbf{u}_g = (-\eta_y, \eta_x)g/f_0$, where g is gravity, η is SSH, and f_0 is the local Coriolis frequency. We define low- and high-pass-filtered velocities thus as

$$\mathbf{u}_K^<(x,y) = \sum_{K'<K} \hat{\mathbf{u}} \exp i(kx + \ell y) \quad \text{and} \tag{5}$$

$$\mathbf{u}_K^>(x,y) = \sum_{K'>K} \hat{\mathbf{u}} \exp i(kx + \ell y), \tag{6}$$

where $K = (k^2 + \ell^2)^{1/2}$ is the isotropic wavenumber and $\hat{\mathbf{u}}$ is the Fourier transform of $\mathbf{u}$. Note that, although K, k, and ℓ are discrete, the above sum treats K' continuously by first masking $\hat{\mathbf{u}}$ with appropriate weights for each K. The low-passed average KE density is $\mathrm{KE}_K^< = \langle \mathbf{u}_K^< \cdot \mathbf{u}_K^< \rangle / 2$, and its evolution is given by [see, e.g., Eqs. (4) and (5) of Scott and Wang 2005]

$$\frac{\partial \mathrm{KE}_K^<}{\partial t} = -\Pi_K + \mathcal{F} - \mathcal{D}, \tag{7}$$

where

$$\Pi_K = \langle \mathbf{u}_K^< \cdot (\mathbf{u}_K^< \cdot \nabla \mathbf{u}_K^>) \rangle + \langle \mathbf{u}_K^< \cdot (\mathbf{u}_K^> \cdot \nabla \mathbf{u}_K^>) \rangle \tag{8}$$

is the flux of energy toward small spectral scales at wavenumber K. Here, $\mathcal{F}$ and $\mathcal{D}$ represent forcing and dissipation terms, respectively. As in Scott and Wang (2005), we assume that the vortex stretching term, which is proportional to $\psi_K^< \partial_z w$ in QG, is contained in the forcing $\mathcal{F}$.

Figure 7 shows spectral fluxes (solid line) and KE spectra (dashed line) at various latitudes plotted against wavenumber (in units of cycles per kilometer). These fluxes and spectra were computed over regions denoted by the overlapping boxes in Fig. 6. That is, one flux is computed within each 10.6° wide box, and then boxes centered at each latitude are zonally averaged, giving equal weight to each box. In each panel, the solid vertical line is K_{bci} and the vertical dashed–dotted line is K_{def}, computed from the climatological atlas and then averaged over the same boxed regions. Note that the fluxes and spectra in each box were first normalized so that each have a maximum (or minimum) value of one before zonal averaging, arriving at an ''equal weighting'' zonal average of scale. This should be contrasted with a nonnormalized zonal average in which longitudes with the highest energy would dominate the average.

Scott and Wang (2005) note that the wavenumber where the spectral energy flux crosses zero can be thought of as the wavenumber of energy injection K_{inj} from which energy cascades to larger scales. We also define the observed eddy wavenumber K_{eddy} as the wavenumber where the KE spectrum peaks, the observed eddy wavelength as $L_{\mathrm{eddy}} = 2\pi K_{\mathrm{eddy}}^{-1}$, and the energy injection wavelength as $L_{\mathrm{inj}} = 2\pi K_{\mathrm{inj}}^{-1}$. The close correspondence between K_{bci} and K_{inj} is pleasing and supports the claim that classic, deep, deformation-scale baroclinic instability energizes eddies in the ACC. The scales of baroclinic instability at lower latitudes are less homogeneous, and observed eddy scales approach the size of the spectral grid in the flux calculations. It is thus difficult to obtain precise estimates of eddy scale in this way. However, L_{bci}, L_{inj}, and L_{eddy} all appear to follow a general trend: they are larger than the deformation scale at higher latitudes and smaller than the deformation scale at lower latitudes.

Scott and Wang (2005) also noted that L_{inj} did not covary with either L_{def} or the Rhines scale $\sqrt{U_{\mathrm{RMS}}/\beta}$. The variation of L_{def} implies too strong a latitudinal dependence: at high latitudes observed scales are greater than L_{def}, whereas at low latitudes they are less than L_{def}. Moreover, because β decreases with latitude and the observed root-mean-square of the eddy velocity does not obviously decrease with latitude outside the tropics (Tulloch et al. 2009), the Rhines scale is unlikely to

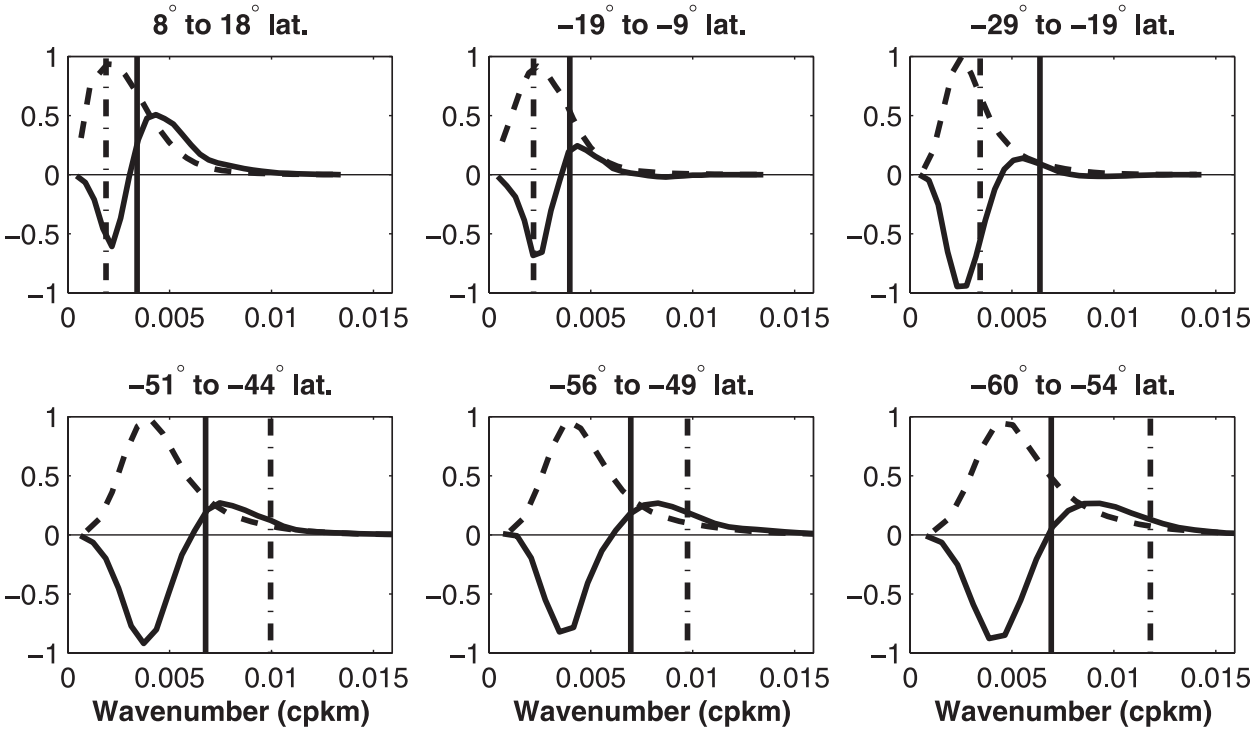

FIG. 7. Spectral flux of KE (solid line) and KE spectrum (dashed line) plotted against total wavenumber (cycles per kilometer) at various latitudes. The vertical solid line is K_{bci}, and the vertical dashed–dotted line is K_{def}.

decrease toward higher latitudes (see, e.g., Fig. 25a of Stammer 1997). If L_{eddy} does not vary with the Rhines scale in the ACC and given that baroclinic instability produces deep modes there, it seems likely that bottom drag may be an important mechanism halting the inverse cascade.

Full zonal averages (away from coastal regions) of L_{def} (dashed black line), L_{inj} (solid black line), L_{bci} (dash-dotted line), and L_{eddy} (gray dotted line) are plotted against latitude in Fig. 8. The eddy scale shown here is a zonal average of the peak wavenumbers of the isotropic KE spectra in each box.[4] At all latitudes, L_{inj} is within about a factor of 2 of L_{eddy}. Similarly, L_{bci} is within a factor of 2–3 of L_{eddy} at all latitudes. Recall that wavenumbers of baroclinic instability are restricted to $K < 5K_{def}$, so it is not surprising that the baroclinic scale is not far from K_{def}. The best match between L_{inj} and L_{bci} is in the ACC from $-60°$ to $-50°$. Here we find deep, first baroclinic instabilities with fast growth rates ($>1/20$ days^{-1}). Again, we see that L_{bci} and L_{eddy} vary less strongly with latitude than L_{def}.

[4] Appendix B discusses the advantages and disadvantages of several different measures of eddy scale and the rationale for this choice of eddy scale.

5. Analysis of global eddying model

To assess the robustness of the observations and calculations presented in the previous section, the same analysis is repeated on an eddy-permitting ocean simulation using an aquaplanet configuration (see Marshall et al. 2007) of the MITgcm (for details of the model's equations and numerical algorithms, see Marshall et al. 1997; Adcroft et al. 2004b).

a. Eddying Double Drake solution

The eddying Double Drake configuration of the MITgcm has nominal grid resolution of about 15–20 km and 41 vertical layers over a 3-km-deep flat-bottomed ocean. There are two meridional land barriers at 90°E and 180°, which extend from the North Pole down to 35°S and create a large, fresh Pacific-like basin; a small, salty Atlantic-like basin; and a circumpolar current in the south (for more details, see Marshall et al. 2007; Ferreira et al. 2010). Atmospheric forcing is provided by steady winds derived from lower-resolution (C24) climatology taken from Ferreira et al. (2010). There is no seasonal cycle or stochastic weather noise to generate mesoscale variability, leaving baroclinic instability as the sole source of variability. The model is initialized with a low resolution (C24) equilibrated ocean state that is

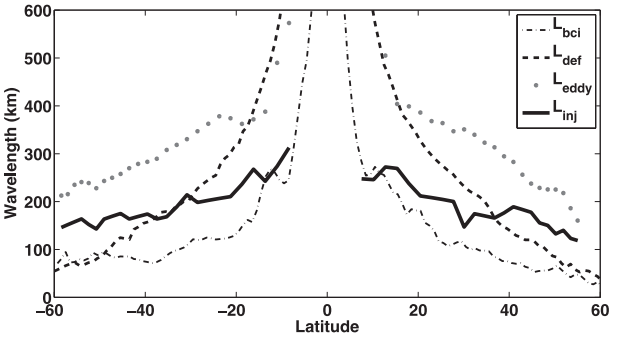

FIG. 8. Full zonal averages of L_{def} (thick dashed black line), L_{inj} (thick solid black line), L_{bci} (dashed–dotted line), and L_{eddy} (gray dotted line); see text for details.

interpolated onto the C510 grid and then spun up for 20 yr, during which time the ocean breaks down into eddies. See appendix C for more details of the configuration.

A snapshot of vorticity ($\zeta = \partial_x v - \partial_y u$) at the surface is shown in Fig. 9. The thick white strip is a land barrier that serves as the eastern (western) boundary of the small (large) basin. The thin white contours mark latitude circles 15° apart. The stability analysis performed here is based on a 5-yr climatology, which is interpolated onto a 1° × 1° grid, the same resolution as the OCCA (Forget 2010).

Salient features of the vorticity field include a linear wave region in the tropics devoid of nonlinear eddies (except at the western boundaries), westward return flows from 15° to 30°N (and from 15° to 30°S), and eastward jets from 30° to 45°N (and from 30° to 45°S). There are also ''dead regions'' largely devoid of eddies, corresponding to flat isopycnals at 45°N and 50°S. Poleward of these regions, eddies are again ubiquitous. The eastward jets appear to be saturated with high values of vorticity as eddies of a uniform scale propagate slowly eastward. Meanwhile, the westward return flows possess large-scale eddies as well as many small-scale filaments, which are barely resolved by the model. Both propagate quickly westward at speeds close to that of the mean flow near the surface. The small filaments in the return flows are surface trapped and are probably SQG like (Tulloch and Smith 2009).

A zonal average of the distribution of eddy kinetic energy (EKE) among the BT and first two BC (BC1 and BC2) vertical modes, defined by Eq. (3), is shown in Fig. 10. The total EKE is

$$\text{EKE} = \frac{1}{H}\int_{-H}^{0} (u')^2 + (v')^2\, dz, \tag{9}$$

where $H = 3$ km and u' and v' are horizontal eddy velocities. Similarly, barotropic and baroclinic EKE are

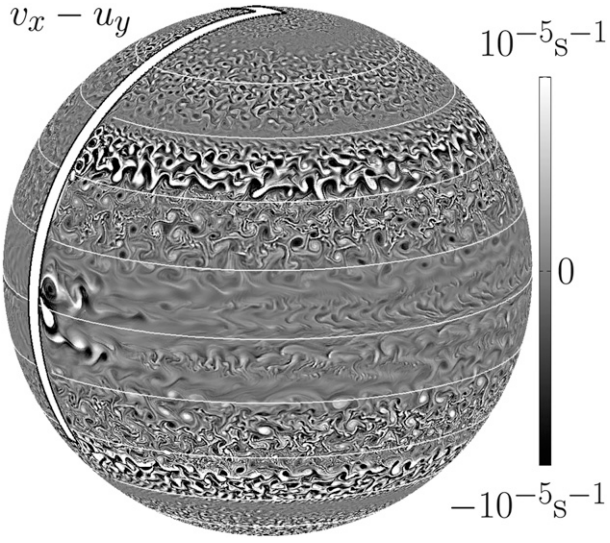

FIG. 9. Snapshot of surface relative vorticity in the eddying Double Drake simulation. The thick, meridional white stripe is the land barrier at the western boundary of the large basin. The thin white zonal stripes denote latitude lines that are spaced by 15°.

$$\text{EKE}_{\text{BT}} = \left(\frac{1}{H}\int_{-H}^{0} u'\, dz\right)^2 + \left(\frac{1}{H}\int_{-H}^{0} v'\, dz\right)^2 \quad \text{and} \tag{10}$$

$$\text{EKE}_{\text{BCj}} = \left(\frac{1}{H}\int_{-H}^{0} \phi_j u'\, dz\right)^2 + \left(\frac{1}{H}\int_{-H}^{0} \phi_j v'\, dz\right)^2, \tag{11}$$

where ϕ_j is the jth vertical mode from Eq. (3). Root-mean-square eddy velocities in the eastward jets are greater than 10 cm s^{-1}, whereas in the return flows they are closer to 5 cm s^{-1}. High latitudes are dominated by BT and BC1 modes. Equatorward of 30°, BC2 becomes increasingly important. Note also that, poleward of 20°, BC1 is the dominant mode, implying that the sea surface

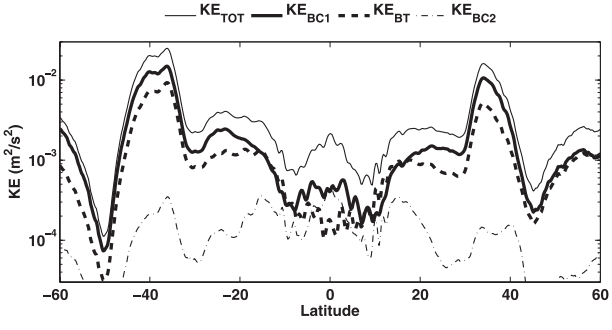

FIG. 10. Zonal averages of vertically integrated EKE (thin solid line), barotropic EKE (thick dashed line), first baroclinic EKE (thick solid line), and second baroclinic EKE (thin dashed–dotted line) plotted against latitude from the Double Drake simulation.

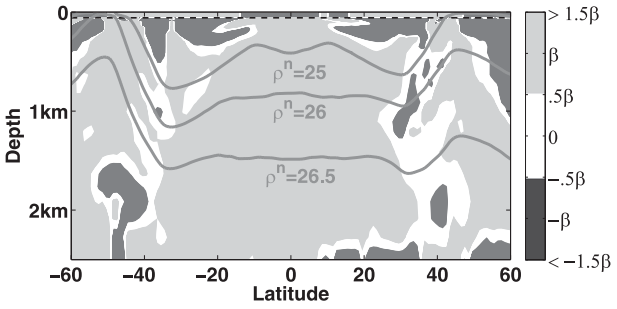

FIG. 11. Cross section of zonally averaged meridional gradient of QGPV $\partial Q/\partial y$ in the Double Drake simulation (in units of the local β). The contribution of the upper surface gradient U_z is shown above 50-m depth. Also plotted are gray contours of neutral density.

height should reflect mostly BC1 dynamics, in agreement with observations (Wunsch 1997).

As might be expected, regions of high and low EKE in Fig. 10 correlate closely with isopycnal slope. Figure 11 shows isopycnals and the QGPV gradient zonally averaged across the large basin. As with Fig. 2, isopycnals sloping up toward the equator in the thermocline are associated with shallow QGPV gradient zero crossings, whereas isopycnals sloping up toward the pole are associated with deep zero crossings, consistent with Smith and Marshall (2009). The trend is more clear in Fig. 11 because the Double Drake simulation is more zonally homogeneous than the ocean.

b. *Baroclinic instability in the Double Drake simulation*

The geography of baroclinic instability in the Double Drake simulation is shown in Fig. 12. Figure 12a shows $\tilde{\omega}_{\text{Eady}}$ and Fig. 12c shows $L_{\text{bci}}/L_{\text{def}}$ at each location. As with the analysis of ocean observations discussed in section 2, baroclinic growth rates are computed on a grid of wavenumbers limited to $K < 5K_{\text{def}}$ to filter out poorly resolved surface instabilities. Figures 12b,d show zonal averages of the same variables (black line) as well as zonally and vertically averaged zonal velocity (red lines). As in the ocean, the highly energetic eastward flows centered near ±40° latitude are dominated by

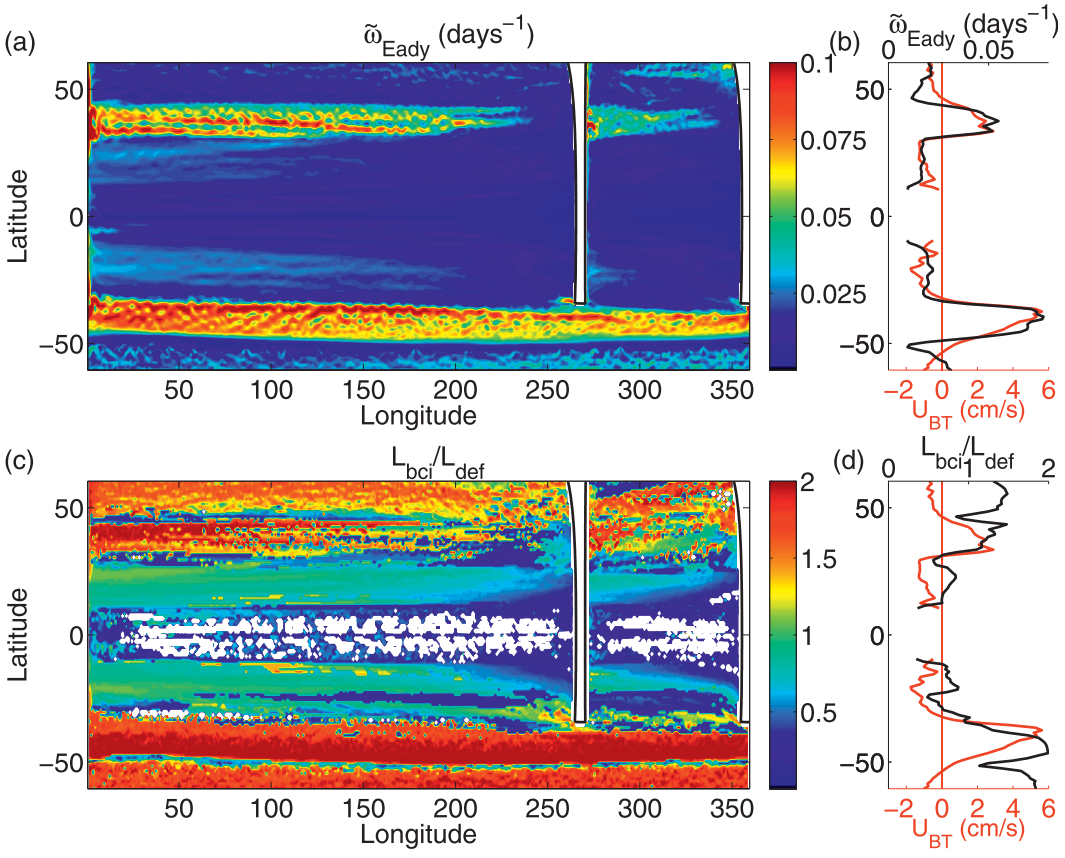

FIG. 12. Global maps and zonal averages of (a),(b) inverse Eady time scale $\tilde{\omega}_{\text{Eady}}$ (days^{-1}) and (c),(d) the ratio $L_{\text{bci}}/L_{\text{def}}$. Zonally and vertically averaged zonal velocity (cm s^{-1}) is plotted in red in (b) and (d) to distinguish low-latitude westward flows from midlatitude eastward flows.

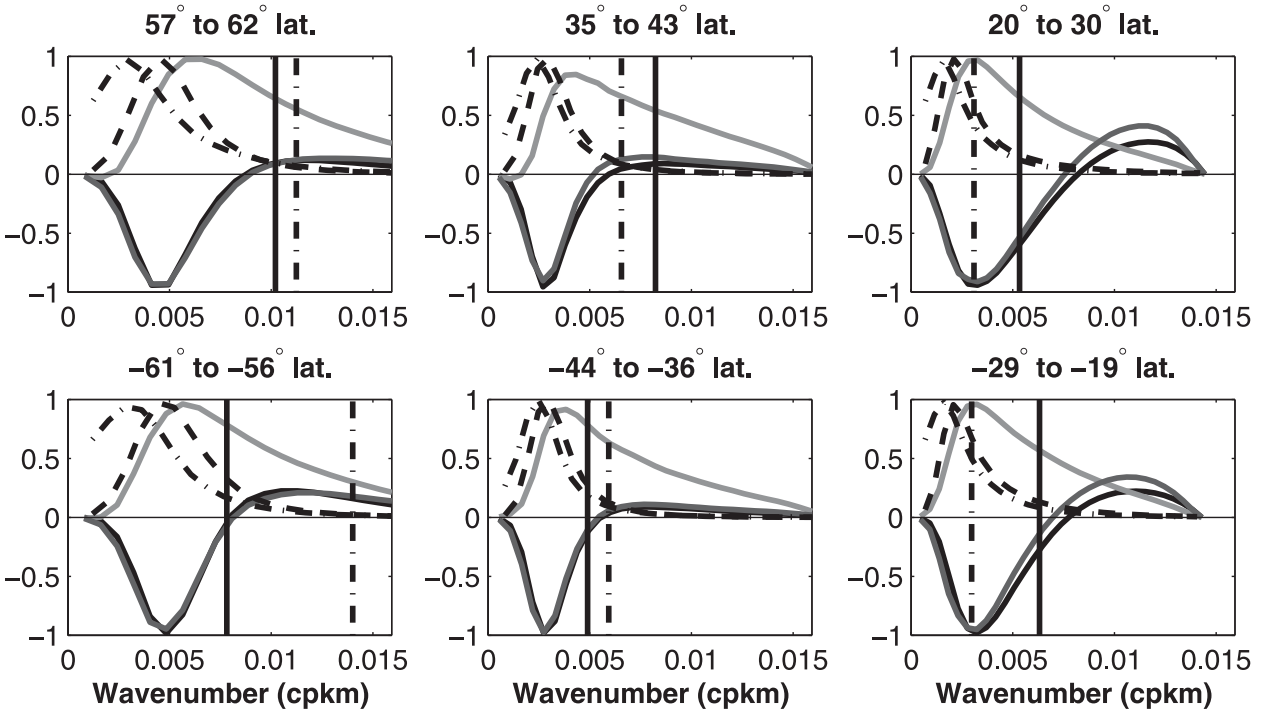

FIG. 13. Zonal averages of normalized surface spectral fluxes and spectra plotted against wavenumber (cycles per kilometer) in the Double Drake simulation. Plotted are the spectral flux of KE computed from SSH gradients (solid black curve), the spectral flux of KE computed from model velocities u and v (dark gray curve), KE spectrum (dashed curve), APE spectrum (dashed–dotted curve), and the spectral flux of APE (gray curve). The vertical solid line is K_{bci}, and the vertical dashed–dotted line is K_{def}.

larger-than-deformation-scale instabilities. Meanwhile, return flows are dominated by smaller-than-deformation-scale instabilities and regions with flat isopycnals are weakly unstable and are associated with very small spatial scales.

c. *Spectral fluxes and eddy scales in the Double Drake simulation*

Unlike the ocean, model KE fluxes of the geostrophic flow can be compared against the fluxes of the full velocity at both the surface and at depth. Not surprisingly, because of the scales permitted and the 10-day velocity averages taken, the geostrophic KE fluxes are very similar to the full KE fluxes. APE fluxes can also be computed from the velocity field and the buoyancy. Following Schlösser and Eden (2007), the APE flux at the surface is

$$B_K = N^{-2}\left\langle b_K^{<}\,\mathbf{u}_K^{<}\cdot\nabla b_K^{>}\right\rangle + N^{-2}\left\langle b_K^{<}\,\mathbf{u}_K^{>}\cdot\nabla b_K^{>}\right\rangle, \tag{12}$$

where $b_K^{<}$ is the low-pass-filtered buoyancy; (u, v) are the model velocities; and a rigid lid $w = 0$ has been assumed.

Figure 13 shows zonally averaged kinetic and APE spectral fluxes and spectra at the surface for various latitude bands. As in Fig. 7, the vertical solid line is the wavenumber of fastest growth K_{bci}, the vertical dashed–dotted line is K_{def}, the dashed curve is the KE spectrum, and the black curve is the spectral flux of KE computed from the SSH gradients. Also plotted in Fig. 13 are the spectral flux of APE (light gray curve), the APE spectrum (dashed–dotted curve) and the spectral flux of KE computed from the model velocities u and v (dark gray curve). In each panel, L_{bci} and L_{def} have been averaged over the latitudes shown and zonally from 20° to 250° and from 290° to 340°. Spectral fluxes of KE computed from velocities are almost identical to those computed from SSH at high latitudes, whereas they have slightly larger forward cascades at lower latitude latitudes. The large forward KE fluxes in the model at low latitudes could also be due to smaller-scale instabilities that are either not present in the ocean or not resolved by the altimeter. The APE flux is robustly positive at all latitudes and scales, consistent with surface geostrophic turbulence theory (Capet et al. 2008). Consistent with the trend in the ocean data, L_{bci} is larger than L_{def} at high latitudes, where instabilities tend to be first baroclinic in vertical structure, and smaller than L_{def} at low latitudes, where instabilities tend to have higher baroclinic vertical structure.

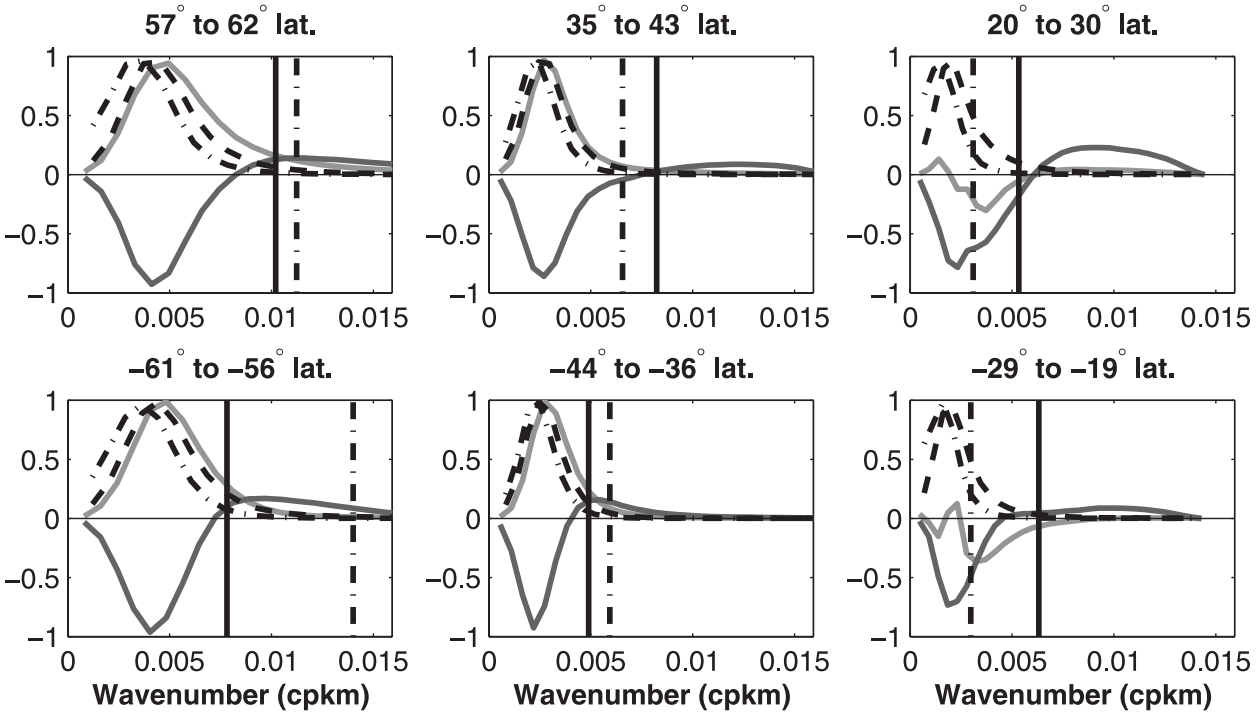

FIG. 14. Zonal averages of normalized spectral fluxes and spectra at 900-m depth, plotted against wavenumber (cycles per kilometer) in the Double Drake simulation. Plotted are the spectral flux of KE computed from model velocities u and v (dark gray curve), KE spectrum (dashed curve), APE spectrum (dashed–dotted curve), and the spectral flux of APE (gray curve). The vertical solid line is K_{bci}, and the vertical dashed–dotted line is K_{bci}.

Figure 14 shows fluxes and spectra analogous to Fig. 13, but at a depth of 900 m. Unlike at the surface where the forward APE flux extends down to the grid scale, in the interior the APE flux tends to zero near K_{inj}, consistent with interior geostrophic turbulence theory, which predicts a flux of APE to deformation scales, followed by a conversion to KE. The zonal averages of the low-latitude (normalized) APE fluxes (Fig. 14, right) peak at amplitudes that are significantly smaller than one, indicating a disagreement in scales across longitudes. However, 900 m is both at the base of the thermocline and below most of the baroclinic growth at these latitudes (recall Fig. 4), so the fluxes there are probably insignificant.

Finally, zonal averages of L_{eddy} (gray dotted line), L_{inj} (thick black line) at the surface, L_{def} (dashed line), and L_{bci} (dashed–dotted line) in the Double Drake simulation are plotted against latitude in Fig. 15. As before, L_{eddy} is a zonal average of the peak wavenumber of the KE spectrum in each 32×32 box. As in the ocean, L_{eddy} varies with latitude in a similar way as L_{def} at higher latitudes, but in the return flows ($\theta < 30°$) it grows with latitude much less than L_{def}. Also, just as in the ocean, there is about a factor of 2–3 between L_{eddy}, L_{bci}, and L_{inj}.

6. Summary and discussion

We remind the reader of the limitations of our simplified analysis. Our use of linear baroclinic instability under the local approximation is not meant to fully explain the generation of oceanic eddies but rather serve as a test of its limits. We have sought to bring together elements of linear and nonlinear geostrophic theory

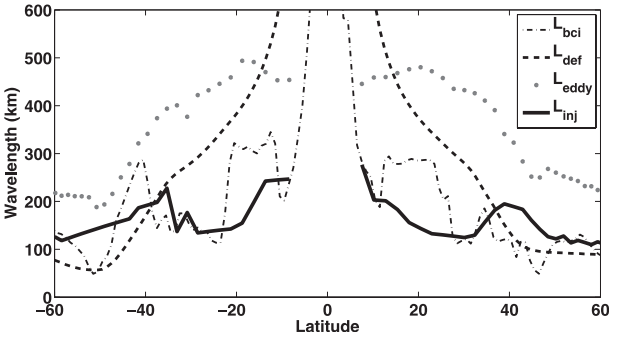

FIG. 15. Zonally averaged eddy scale (gray dotted line), deformation scale (dashed line), energy injection scale (thick line), and the scale of maximum baroclinic growth rate (dashed–dotted line) in the Double Drake simulation as defined in sections 3 and 4.

using both ocean data and a model simulation. The four main results of our study are as follows: 1) in zonal flow, there is an asymmetry between regions of eastward flows which tend to have deep zero crossings in the meridional QGPV gradient, and westward return flows, which are associated with shallow zero crossings in the QGPV gradient; 2) L_{eddy} and L_{bci} predicted by linear theory both vary less strongly with latitude than L_{def}; 3) the inverse cascade throughout the ocean spans a modest range of scales; and 4) these aforementioned features can be captured in an idealized eddying GCM with no atmospheric variability and a flat bottom.

The tendency toward shallow zero crossings of the QGPV gradient in regions where the thermocline slopes equatorward is a consequence of the reversal of the meridional density gradient between the thermocline and the surface. Such regions tend to exhibit Charney-type baroclinic instability on horizontal scales between the first and second baroclinic wavenumbers. Steering levels, which were not shown here but will be discussed in a future paper, also tend to be shallow in these regions because the barotropic component of the mean zonal flow usually reinforces the tendency of mesoscale anomalies to propagate westward. In regions where the thermocline slopes poleward, the zero crossing of the QGPV gradient is below the maximum isopycnal slope, which tends to be near the depth of the thermocline. Steering levels also tend to be deep in such regions.

One of the key results of the baroclinic instability analysis performed here is that L_{bci} in the ACC is often larger than L_{def} there (see Fig. 6). The growth rates of such instabilities are on the order of 10 days and are only rivaled by very small-scale surface instabilities (which are arguably not resolved by such a climatological analysis). Eastward wind-driven jets in the Double Drake simulation exhibit similarly large growth rates and scales (see Fig. 12).

The oceanic inverse cascade is a subject of much debate. We find evidence of only a modest inverse cascade especially in the eddy-rich regions driven by larger-than-deformation-scale instabilities. In mixed shear return flows baroclinic instability acts closer to the surface at scales smaller than L_{def}, but L_{eddy} in those lower latitude regions are also smaller relative to L_{def}.

Acknowledgments. This study was supported by grants from NSF and NOAA.

APPENDIX A

Baroclinic Instability in Other Ocean Atlases

To compare the OCCA with more traditional ocean atlases, we show growth rates and length scales of maximum baroclinic instability in the World Ocean Circulation Experiment (WOCE) 2004 climatology (Gouretski and Koltermann 2004) and the *World Ocean Atlas 2005* (*WOA05*) climatology (Boyer et al. 2006). The WOCE climatology uses data optimally interpolated onto a $0.5° \times 0.5°$ grid with 45 vertical levels, whereas the *WOA05* climatology is interpolated onto a $1° \times 1°$ grid with 33 vertical levels. All modern climatologies appear to suffer from a lack of observations at depths below 1.5 km in the Southern Ocean, so the GCM-interpolated OCCA is likely more suitable for instability calculations there.

Figure A1 shows baroclinic growth rates in WOCE and *WOA05*, which are directly comparable to Fig. 5b. Outside the tropics, the two agree with each other very well and with the OCCA. The WOCE climatology has more finescale instability because it is on a finer grid. The WOCE climatology is also noisier than OCCA, which tends to create larger growth rates.

Figure A2 shows length scales of maximum baroclinic instability nondimensionalized by the local deformation scale in WOCE and *WOA05*, comparable to Fig. 6a. The broad features are consistent in all three datasets, but the OCCA is substantially less noisy, particularly in the ACC.

Smith (2007b) analyzed the WOCE climatology and found quite different scales and growth rates than those reported here (specifically, smaller and faster). This is due to an unfortunate gridding mistake in Smith's analysis, which followed from an error on p. 22 of Gouretski and Koltermann (2004). Specifically, the vertical grid levels are listed in Gouretski and Koltermann (2004) as including data at 450 m and not at 900 m, whereas the climatology in fact included data at 900 m but not at 450 m. This led to kinks in the profiles of stratification and shear, resulting in unphysical instabilities. The discovery of this error came about as the result of the present analysis.

APPENDIX B

Estimates of Eddy Length Scale

Various measures exist for the length scale of eddies. For example, Stammer (1997) used autocorrelation of SSH gradients as well as cross-track (mainly zonal) spectral peaks. Eden (2007) used Stammer's autocorrelation measures and measures based on moments of isotropic KE. The simplest measure of scale is the peak wavenumber of the isotropic KE spectrum. However, because isotropic spectra are computed from two-dimensional grid boxes, eddies with scales near the box size become coarsely quantized. For this reason, measures

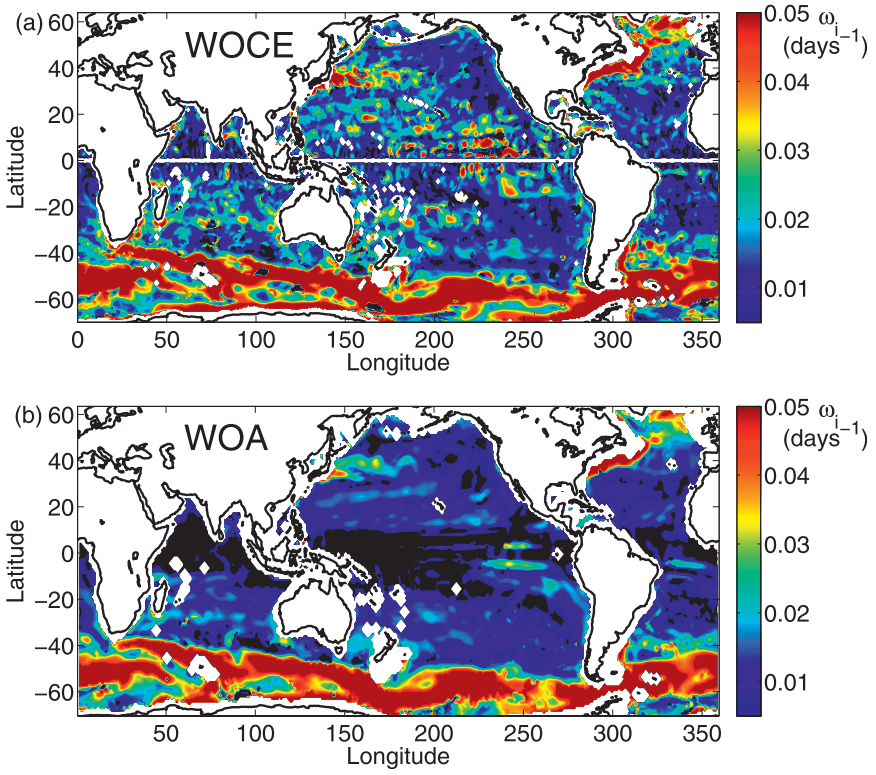

FIG. A1. Baroclinic growth rate ω_i (days^{-1}) in (a) the WOCE 2004 climatology (Gouretski and Koltermann 2004) and (b) the *WOA05* climatology (Boyer et al. 2006). Growth rates less than $^1/_{200}$ days^{-1} are shaded black, and locations with no data are white.

based on moments of the KE spectrum, such as the centroid

$$K^c = \frac{\sum K \cdot \mathrm{KE}(K)}{\sum \mathrm{KE}(K)}, \tag{B1}$$

are often used instead of the peak wavenumber. However, such measures depend on spectral slopes, measurement noise, and data interpolation.

Figure B1 shows four zonally averaged measures of eddy scale (gray lines) and the deformation scale (dashed line) in the ocean plotted against latitude. The gray Xs are the wavelengths corresponding to the centroid wavenumber K^c, and the gray circles are the wavelengths of the peak wavenumber of the KE spectra. The solid gray line is $L_{\mathrm{SW}} = 2\pi/K^c$, computed in the Pacific by Scott and Wang (2005) in roughly the same way as done here. The relative difference between Scott's scales and the centroid computed here is slight, never more than about 5%, and likely only the result of minor technical differences. The dashed gray line is a measure of eddy scale computed from contours of the Okubo–Weiss parameter by Chelton et al. (2007). In their analysis, they compute the Okubo–Weiss parameter, $W = 4(u_x^2 + v_x u_y)$, from SSH gradients and define eddies as having either wholly positive or negative SSH within regions where $W < -2 \times 10^{-12}$ s^{-2}. From these eddy regions, they compute diameters of circles that cover the same area. The gray dashed line L_{chelton} in Fig. B1 is a zonal average of twice the eddy diameters computed by Chelton et al. (2007), which assumes that a wavelength is comprised of two adjacent diameters of alternate sign.

All of the scales shown in Fig. B1 lie within a wavelength range that is less than 100 km wide at any given latitude, and their dependence against latitude is less strong than that of the deformation wavelength. The zonal average of the peak wavenumber (dotted gray line) is consistent with the other measures and is therefore the measure that is plotted in Fig. 8.

APPENDIX C

Double Drake Model Configuration

The eddying Double Drake model employs a cube sphere configuration (Ronchi et al. 1996; Rancic et al. 1996; Adcroft et al. 2004a) of the MITgcm. The mesh is locally orthogonal with 510 grid cells along each edge of

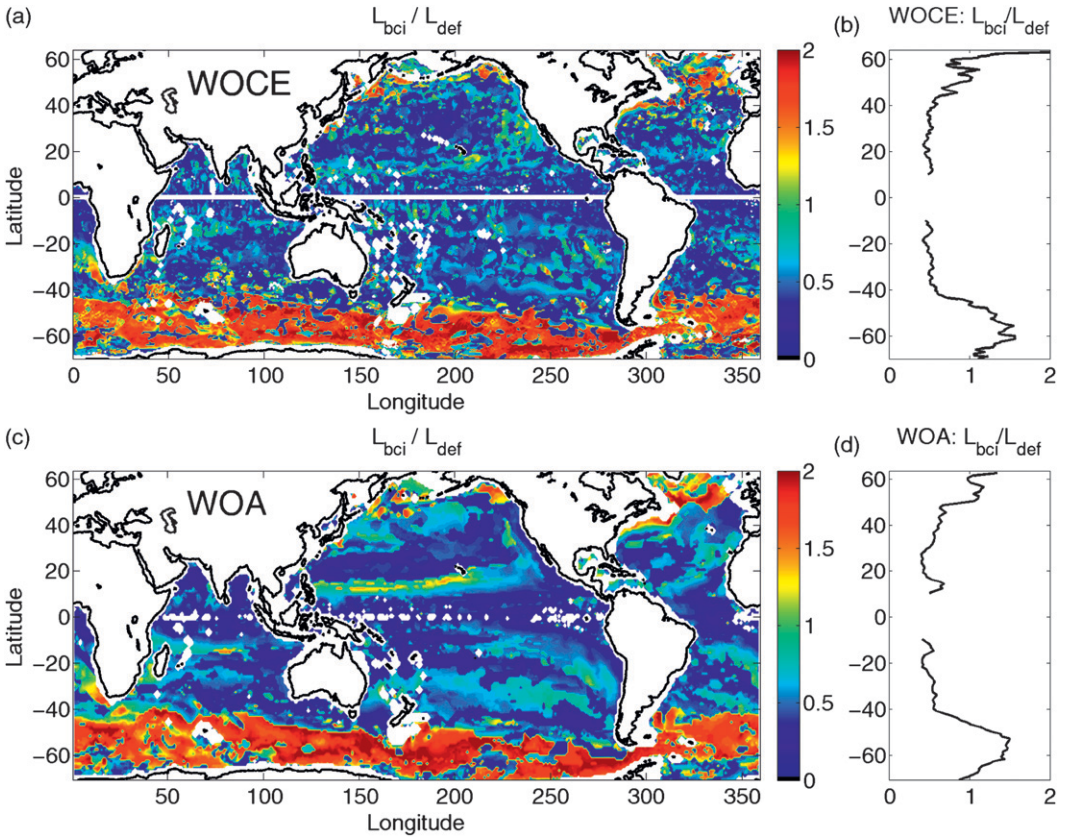

FIG. A2. Values of L_{bci}/L_{def} in (a) the WOCE 2004 climatology (Gouretski and Koltermann 2004) and (b) the *WOA05* climatology (Boyer et al. 2006). Regions with no data or where no maximum was found within $K < 5K_{def}$ are white.

the cube faces. The distribution of cell corners along cube face edges follows the tan function used in Menemenlis et al. (2005), which produces isotropic cell edge lengths. The maximum cell edge length is 25 km, the mean cell edge length is 18 km, and the minimum length is 4 km (at the cube corner points). This model configuration integrates the hydrostatic equations with a fully nonlinear equation of state (Jackett and McDougall 1995; McDougall et al. 2003).

Horizontal vorticity is advected according to a fourth-order accurate spatial discretization using an enstrophy conserving (Arakawa and Lamb 1977) and vector invariant formulation. Horizontal viscosity is biharmonic, with an amplitude that scales according to local grid spacing and stresses (Fox-Kemper and Menemenlis 2008). Vertical viscosity is Laplacian, flow alongside walls is zero, and a bottom drag term is imposed at the flat bottom in the lowest model layer. The vertical coordinate is a scaled, height-based coordinate in which vertical layer thicknesses scale in proportion with barotropic mode amplitude (Adcroft and Campin 2004) and a nonlinear free surface term balance is implemented (Campin et al. 2004).

Momentum (and temperature and salinity) is forced at the surface by climatological fields from a coarse-resolution experiment with the same ocean geometry (Ferreira et al. 2010). The initial hydrography is taken from the same coarse-resolution setup. There is no

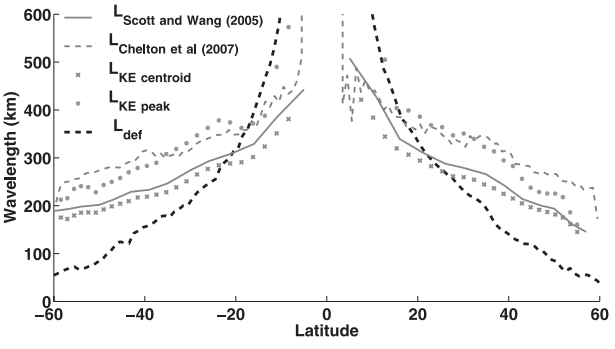

FIG. B1. Full zonal averages of L_{def} (thick dashed black lines) and measures of L_{eddy} (gray lines) based on the centroid of KE (this calculation can be compared to Scott and Wang 2005), the peak of the KE spectrum, and the Okubo–Weiss parameter from Chelton et al. (2007).

TABLE C1. Numerical parameters used in the eddying Double Drake simulation.

Parameter	Value
Level depths (m)	5, 15, 25, 35, 45, 55, 65, 75, 85, 95, 105, 115, 127, 139, 154, 172, 194, 222, 257, 299, 350, 409, 477, 552, 634, 722, 814, 909, 1007, 1105, 1205, 1306, 1409, 1517, 1634, 1765, 1914, 2084, 2276, 2491, 2802
Vertical viscosity ($m^2\ s^{-2}$)	10^{-3}
Side boundary	No slip
Bottom boundary	No slip
Linear bottom drag (s^{-1})	10^{-2}
Quadratic bottom drag (s^{-2})	2.1×10^{-3}
Time step (s)	600
Mean horizontal grid spacing (m)	1.8×10^{-4}
Shear instability critical Richardson number	0.358

explicit sea ice; instead, temperatures are clamped at $\theta > -1.9$°C. Advection of temperature, salinity, and passive tracers utilizes a spatially seventh-order accurate, monotonicity preserving scheme (Daru and Tenaud 2004).

The K-profile parameterization scheme of Large et al. (1994) is used to parameterize vertical mixing due to boundary layer shear and/or convective instability. Table C1 summarizes the numerical parameters employed.

REFERENCES

Adcroft, A., and J.-M. Campin, 2004: Re-scaled height coordinates for accurate representation of free-surface flows in ocean circulation models. *Ocean Modell.,* **7,** 269–284.

——, ——, C. Hill, and J. Marshall, 2004a: Implementation of an atmosphere–ocean general circulation model on the expanded spherical cube. *Mon. Wea. Rev.,* **132,** 2845–2863.

——, C. Hill, J. Marshall, and P. Heimbach, 2004b: Overview of the formulation and numerics of the MIT GCM. *Proceedings of the ECMWF: Seminar Series on Numerical Methods, Recent Developments in Numerical Methods for Atmosphere and Ocean Modelling,* ECMWF, 139–149.

Arakawa, A., and V. Lamb, 1977: Computational design of the basic dynamical processes of the UCLA general circulation model. *General Circulation Models of the Atmosphere,* B. Adler, Ed., Vol. 17, *Methods in Computational Physics,* Academic Press, 174–267.

Arbic, B. K., 2000: Generation of mid-ocean eddies: The local baroclinic instability hypothesis. Ph.D. thesis, Massachusetts Institute of Technology and Woods Hole Oceanographic Institution, 289 pp.

——, and G. R. Flierl, 2004: Effects of mean flow direction on energy, isotropy, and coherence of baroclinically unstable beta-plane geostrophic turbulence. *J. Phys. Oceanogr.,* **34,** 77–93.

Boyer, T. P., and Coauthors, 2006: *Introduction*. Vol. 1, *World Ocean Database 2005,* NOAA Atlas NESDIS 60, 190 pp.

Bretherton, F. P., 1966: Critical layer instability in baroclinic flows. *Quart. J. Roy. Meteor. Soc.,* **92,** 325–334.

Campin, J.-M., A. Adcroft, J. Marshall, and C. Hill, 2004: Conservation properties in a free surface ocean model. *Ocean Modell.,* **6,** 221–244.

Capet, X., P. Klein, B. L. Hua, G. Lapeyre, and J. C. McWilliams, 2008: Surface kinetic energy transfer in surface quasi-geostrophic flows. *J. Fluid Mech.,* **604,** 165–174.

Charney, J. G., 1947: Dynamics of long waves in a baroclinic westerly current. *J. Meteor.,* **4,** 135–162.

——, and M. E. Stern, 1962: On the stability of internal baroclinic jets in a rotating atmosphere. *J. Atmos. Sci.,* **19,** 159–172.

Chelton, D. B., M. G. Schlax, R. M. Samelson, and R. A. de Szoeke, 2007: Global observations of large oceanic eddies. *Geophys. Res. Lett.,* **34,** L15606, doi:10.1029/2007GL030812.

Daru, V., and C. Tenaud, 2004: High order one-step monotonicity-preserving schemes for unsteady compressible flow calculations. *J. Comput. Phys.,* **193,** 563–594.

Eady, E. T., 1949: Long waves and cyclone waves. *Tellus,* **1,** 33–52.

Eden, C., 2007: Eddy length scales in the North Atlantic Ocean. *J. Geophys. Res.,* **112,** C06004, doi:10.1029/2006JC003901.

Farrell, B., and P. Ioannou, 1999: Perturbation growth and structure in time-dependent flows. *J. Atmos. Sci.,* **56,** 3622–3639.

Ferrari, R., and C. Wunsch, 2009: Ocean circulation kinetic energy: Reservoirs, sources, and sinks. *Annu. Rev. Fluid Mech.,* **41,** 253–282.

Ferreira, D., J. Marshall, and J.-M. Campin, 2010: Localization of deep water formation: Role of atmospheric moisture transport and geometrical constraints on ocean circulation. *J. Climate,* **23,** 1456–1476.

Flierl, G. R., and J. Pedlosky, 2007: The nonlinear dynamics of time-dependent subcritical baroclinic currents. *J. Phys. Oceanogr.,* **37,** 1001–1021.

Forget, G., 2010: Mapping ocean observations in a dynamical framework: A 2004–06 ocean atlas. *J. Phys. Oceanogr.,* **40,** 1201–1221.

Fox-Kemper, B., and D. Menemenlis, 2008: Can large eddy simulation techniques improve mesoscale rich ocean models? *Ocean Modeling in an Eddying Regime, Geophys. Monogr.,* Vol. 177, Amer. Geophys. Union, 319–337.

Frankignoul, C., and P. Müller, 1979: Quasi-geostrophic response of an infinite beta-plane ocean to stochastic forcing by the atmosphere. *J. Phys. Oceanogr.,* **9,** 104–127.

Frisch, U., 1995: *Turbulence: The Legacy of A. N. Kolmogorov*. 1st ed. Cambridge University Press, 296 pp.

Gill, A. E., J. S. A. Green, and A. J. Simmons, 1974: Energy partition in the large-scale ocean circulation and the production of mid-ocean eddies. *Deep-Sea Res.,* **21,** 499–528.

Gouretski, V. V., and K. P. Koltermann, 2004: WOCE global hydrographic climatology. Berichte des Bundesamtes für Seeschifffahrt und Hydrographie Tech. Rep. 35, 52, pp.

Green, J. S. A., 1960: A problem in baroclinic instability. *Quart. J. Roy. Meteor. Soc.,* **86,** 237–251.

Halliwell, G., G. Peng, and D. B. Olson, 1994: Stability of the Sargasso Sea subtropical frontal zone. *J. Phys. Oceanogr.,* **24,** 1166–1183.

Hart, J. E., 1981: Wavenumber selection in nonlinear baroclinic instability. *J. Atmos. Sci.,* **38,** 400–408.

Held, I. M., and V. D. Larichev, 1996: A scaling theory for horizontally homogeneous, baroclinically unstable flow on a beta plane. *J. Atmos. Sci.,* **53,** 946–952.

——, R. T. Pierrehumbert, S. T. Garner, and K. L. Swanson, 1995: Surface quasi-geostrophic dynamics. *J. Fluid Mech.,* **282,** 1–20.

Hristova, H. G., J. Pedlosky, and M. A. Spall, 2008: Radiating instability of a meridional boundary current. *J. Phys. Oceanogr.,* **38,** 2294–2307.

Jackett, D. R., and T. J. McDougall, 1995: Minimal adjustment of hydrographic profiles to achieve static stability. *J. Atmos. Oceanic Technol.,* **12,** 381–389.

Kamenkovich, I. V., and J. Pedlosky, 1996: Radiating instability of nonzonal ocean currents. *J. Phys. Oceanogr.,* **26,** 622–643.

Killworth, P. D., and J. R. Blundell, 2007: Planetary wave response to surface forcing and to instability in the presence of mean flow and topography. *J. Phys. Oceanogr.,* **37,** 1297–1320.

Kobashi, F., and H. Kawamura, 2002: Seasonal variation and instability nature of the North Pacific Subtropical Countercurrent and the Hawaiian Lee Countercurrent. *J. Geophys. Res.,* **107,** 3185, doi:10.1029/2001JC001225.

Lapeyre, G., 2009: What vertical mode does the altimeter reflect? On the decomposition in baroclinic modes and on a surface-trapped mode. *J. Phys. Oceanogr.,* **39,** 2857–2874.

Large, W. G., W. R. Holland, and J. C. Evans, 1991: Quasi-geostrophic ocean response to real wind forcing: The effects of temporal smoothing. *J. Phys. Oceanogr.,* **21,** 998–1017.

——, J. McWilliams, and S. Doney, 1994: Oceanic vertical mixing: A review and a model with nonlocal boundary layer parameterization. *Rev. Geophys.,* **32,** 363–403.

Le Traon, P. Y., F. Nadal, and N. Ducet, 1998: An improved mapping method of multisatellite altimeter data. *J. Atmos. Oceanic Technol.,* **15,** 522–534.

Marotzke, J., R. Giering, K. Q. Zhang, D. Stammer, C. Hill, and T. Lee, 1999: Construction of the adjoint MIT ocean general circulation model and application to Atlantic heat transport variability. *J. Geophys. Res.,* **104** (C12), 29 529–29 547.

Marshall, J., A. Adcroft, C. Hill, L. Perelman, and C. Heisey, 1997: A finite-volume, incompressible Navier Stokes model for studies of the ocean on parallel computers. *J. Geophys. Res.,* **102,** 5753–5766.

——, D. Ferreira, J.-M. Campin, and D. Enderton, 2007: Mean climate and variability of the atmosphere and ocean on an aquaplanet. *J. Atmos. Sci.,* **64,** 4270–4286.

McDougall, T. J., D. R. Jackett, D. G. Wright, and R. Feistel, 2003: Accurate and computationally efficient algorithms for potential temperature and density of seawater. *J. Atmos. Oceanic Technol.,* **20,** 730–741.

Menemenlis, D., and Coauthors, 2005: NASA supercomputer improves prospects for ocean climate research. *Eos, Trans. Amer. Geophys. Union,* **86,** doi:10.1029/2005EO090002.

Pedlosky, J., 1964: The stability of currents in the atmosphere and ocean. Part I. *J. Atmos. Sci.,* **21,** 201–219.

——, 1981: The nonlinear dynamics of baroclinic wave ensembles. *J. Fluid Mech.,* **102,** 169–209.

——, 1987: *Geophysical Fluid Dynamics*. 2nd ed. Springer-Verlag, 710 pp.

Phillips, N. A., 1954: Energy transformations and meridional circulations associated with simple baroclinic waves in a two-level, quasi-geostrophic model. *Tellus,* **6,** 273–286.

Qiu, B., 1999: Seasonal eddy field modulation of the North Pacific Subtropical Countercurrent: TOPEX/Poseidon observations and theory. *J. Phys. Oceanogr.,* **29,** 2471–2486.

——, R. B. Scott, and S. Chen, 2008: Length scales of eddy generation and nonlinear evolution of the seasonally modulated South Pacific Subtropical Countercurrent. *J. Phys. Oceanogr.,* **38,** 1515–1528.

Rancic, M., R. Purser, and F. Mesinger, 1996: A global shallow-water model using an expanded spherical cube: Gnomic versus conformal coordinates. *Quart. J. Roy. Meteor. Soc.,* **122,** 959–982.

Robinson, A., and J. McWilliams, 1974: The baroclinic instability of the open ocean. *J. Phys. Oceanogr.,* **4,** 281–294.

Ronchi, C., R. Iacono, and P. S. Paolucci, 1996: The ''cubed sphere'': A new method for the solution of partial differential equations in spherical geometry. *J. Comput. Phys.,* **124,** 93–114, doi:10.1006/jcph.1996.0047.

Schlösser, F., and C. Eden, 2007: Diagnosing the energy cascade in a model of the North Atlantic. *Geophys. Res. Lett.,* **34,** L02604, doi:10.1029/2006GL027813.

Scott, R. B., and F. Wang, 2005: Direct evidence of an oceanic inverse kinetic energy cascade from satellite altimetry. *J. Phys. Oceanogr.,* **35,** 1650–1666.

Smith, K. S., 2007a: Eddy amplitudes in baroclinic turbulence driven by nonzonal mean flow: Shear dispersion of potential vorticity. *J. Phys. Oceanogr.,* **37,** 1037–1050.

——, 2007b: The geography of linear baroclinic instability in Earth's oceans. *J. Mar. Res.,* **65,** 655–683.

——, and J. Marshall, 2009: Evidence for enhanced eddy mixing at middepth in the Southern Ocean. *J. Phys. Oceanogr.,* **39,** 1037–1050.

Spall, M. A., 2000: Generation of strong mesoscale eddies by weak ocean gyres. *J. Mar. Res.,* **58,** 97–116.

Stammer, D., 1997: Global characteristics of ocean variability estimated from regional TOPEX/Poseidon altimeter measurements. *J. Phys. Oceanogr.,* **27,** 1743–1769.

——, and C. Wunsch, 1999: Temporal chances in the mesoscale variability of the oceans. *Deep-Sea Res. II,* **46,** 77–108.

Stone, P. H., 1966: On non-geostrophic baroclinic instability. *J. Atmos. Sci.,* **23,** 390–400.

Tulloch, R., and K. S. Smith, 2009: A note on the numerical representation of surface dynamics in quasigeostrophic turbulence: Application to the nonlinear Eady model. *J. Atmos. Sci.,* **66,** 1063–1068.

——, J. Marshall, and K. S. Smith, 2009: Interpretation of the propagation of surface altimetric observations in terms of planetary waves and geostrophic turbulence. *J. Geophys. Res.,* **114,** doi:10.1029/2008JC005055.

Visbeck, M., J. Marshall, T. Haine, and M. Spall, 1997: Specification of eddy transfer coefficients in coarse-resolution ocean circulation models. *J. Phys. Oceanogr.,* **27,** 381–402.

Walker, A., and J. Pedlosky, 2002: Instability of meridional baroclinic currents. *J. Phys. Oceanogr.,* **32,** 1075–1093.

Wunsch, C., 1997: The vertical partition of oceanic horizontal kinetic energy. *J. Phys. Oceanogr.,* **27,** 1770–1794.